Coupling of continuous and hybridizable discontinuous Galerkin methods

Application to conjugate heat transfer problem

Mahendra Paipuri · Carlos Tiago · Sonia Fernández–Méndez

Abstract A coupling strategy between hybridizable discontinuous Galerkin (HDG) and continuous Galerkin (CG) methods is proposed in the framework of second-order elliptic operators. The coupled formulation is implemented and its convergence properties are established numerically by using manufactured solutions. Afterwards, the solution of the coupled Navier–Stokes/convection-diffusion problem, using Boussinesq approximation, is formulated within the HDG framework and analysed using numerical experiments. Results of Rayleigh–Bénard convection flow are also presented and validated with literature data. Finally, the proposed coupled formulation between HDG and CG for heat equation is combined with the coupled Navier–Stokes/convection diffusion equations to formulate a new CG-HDG model for solving conjugate heat transfer problems. Benchmark examples are solved using the proposed model and validated with literature values. The proposed CG-HDG model is also compared with a CG-CG model, where all the equations are discretized using the CG method, and it is concluded that CG-HDG model can have a superior computational efficiency when compared to CG-CG model.

Keywords hybridizable discontinuous Galerkin · continuous Galerkin · coupling · Navier–Stokes · convection-diffusion · conjugate heat transfer

Mahendra Paipuri, Carlos Tiago
CEris, ICIST, Instituto Superior Técnico,
Universidade de Lisboa, Av. Rovisco Pais,
1049-001 Lisboa, Portugal.
E-mail: {mahendra.paipuri, carlos.tiago}@tecnico.ulisboa.pt

Sonia Fernández–Méndez
Laboratori de Càlcul Numèric (LaCàN),
Universidad Politècnica de Catalunya,
Campus Nord, 08034 Barcelona, Spain.
E-mail: sonia.fernandez@upc.edu

1 Introduction

Conjugate heat transfer problem describes the variations of temperature in fluid and solid domains in a coupled system. In solids, conduction is the dominant phenomenon, whereas in fluids, convection usually prevails. There are plenty of applications of conjugate heat transfer models [19], like designing effective heat exchangers, forced convection regimes, *etc.* The temperature variation in solid is described by the heat conduction equation, whereas the fluid's is described by Navier–Stokes and energy equations. The solution of these problems, however, is far from trivial as convection dominated regimes in fluids may develop sharp fronts and boundary layers. In solids, the solution to the conduction equation is relatively smooth in the absence of strong non-linearities in the material properties, which can depend on temperature.

Continuous Galerkin (CG) finite element methods are widely used in computational mechanics. However, for convection dominated problems, CG methods might pose stability issues. Discontinuous Galerkin (DG) finite element methods, originally developed for hyperbolic equations [41], offer some interesting features in this context: (i) local conservation, as they are based on satisfying conservation principles element-by-element, (ii) ability to handle hanging nodes, thereby making the implementation of adaptive algorithms relatively easier and (iii) ready parallelization. However, DG methods for problems involving self-adjoint operators, such as Interior Penalty Methods (IPM) [5], Local Discontinuous Galerkin (LDG) methods [13] and Compact Discontinuous Galerkin (CDG) methods [39] are often criticised for having a higher number of degrees of freedoms (DOFs).

With the introduction of Hybridizable Discontinuous Galerkin (HDG) methods [11] in the framework of second-order elliptic problems, the mentioned drawback of the DG methods is addressed. The hybridization technique in the case of HDG methods leads to significant reduction in number of DOFs in the final system. HDG method have also been successfully applied to Navier–Stokes problems [35] and convection-diffusion equations [10] providing stable solutions in convection dominated problems, with a very competitive number of DOFs when compared to CG methods [37].

This manuscript proposes two coupled CG-HDG formulations for the solution of conjugate heat transfer problems. A HDG discretization is considered for the fluid domain, taking advantage of the superior stability properties of DG methods, while keeping a competitive DOF count. A CG formulation is considered for the discretization of the heat equation in the solid domain, where no stabilization is required. Both formulations are set together with a proper coupled weak form.

Several formulations coupling CG with DG methods have been proposed in the literature: for the simulation of rotating electrical machines, motivated by the ability of DG methods to handle hanging nodes on non-matching interfaces [2], for second-order elliptic problems [40], for shallow water problems [15,16,17,7], for poroelasticity with an adaptive penalty scheme [31], and for advection-diffusion-reaction problems [8], among others. The LDG

method has been coupled to CG formulations for transport problems [14] and for convection-diffusion problems in [51,50,49].

As far as the knowledge of the authors, coupled CG-HDG scheme has not been proposed yet in any framework. Hence, the present work focuses on the coupling of HDG with CG in the context of conjugate heat transfer problems, aiming to combine the favourable features of both CG and HDG methods. To accomplish this goal, a coupled formulation with HDG in the fluid domain and CG in the solid domain is first developed for the steady state heat equation in section 3. Then, a HDG formulation for the coupled Navier–Stokes and convection-diffusion equations in the fluid domain is presented and analysed numerically, in section 4. Finally, in section 5, the HDG formulation for the fluid domain is coupled, through the convection-diffusion equation, to the heat transfer equation in the solid domain, to solve conjugate heat transfer problems.

2 Notation

Most of the algebra presented in this text is expressed in symbolic (also frequently referred to as direct, intrinsic or absolute) notation [24]. The usual matrix and indicial notation are sometimes employed in specific cases.

Throughout the text italic Latin or Greek lowercase letters $(a, b, \ldots \alpha, \beta, \ldots)$ denote scalar quantities, bold italic Latin or Greek lowercase letters $(\boldsymbol{a}, \boldsymbol{b}, \ldots \boldsymbol{\alpha}, \boldsymbol{\beta}, \ldots)$ denote vectors and bold italic Latin or Greek capital letters $(\boldsymbol{A}, \boldsymbol{B}, \ldots)$ denote second-order tensors in a d-dimensional Euclidean space.

Rectangular and single-column matrices built of tensor components on orthogonal frames are expressed by boldface upright Latin or Greek letters $(\mathbf{A}, \mathbf{B}, \ldots \mathbf{a}, \mathbf{b} \ldots \boldsymbol{\rho}, \boldsymbol{\lambda} \ldots)$. The scalar products used in the present paper are $(\cdot,\cdot)_D$ and $\langle \cdot,\cdot \rangle_B$, which represents the $\mathcal{L}_2$ scalar product in any domain, D, and over any boundary, B, respectively. Let the domain, Ω, be split into two subdomains, Ω_D and Ω_C, such that $\bar{\Omega} = \bar{\Omega}_D \cup \bar{\Omega}_C$ with an interface $\Gamma_I = \bar{\Omega}_D \cap \bar{\Omega}_C$, as shown in fig. 1. In this work, HDG discretization will be considered in Ω_D, and CG formulation is stated in Ω_C. The domain Ω is assumed to be divided into n_{el} elements, Ω^e, with the boundaries $\partial\Omega^e$.

$$\bar{\Omega} = \bigcup_{e=1}^{n_{el}} \bar{\Omega}^e, \quad \Omega^e \cap \Omega^k = \emptyset \quad \text{for} \quad e \neq k, \tag{1}$$

The elements in Ω_D and Ω_C are represented as Ω_D^e and Ω_C^e, respectively, while the exterior boundaries are denoted by Γ_D and Γ_C, respectively. The union of all faces in Ω_D is denoted as

$$\Gamma = \bigcup_{e=1}^{m_{el}} \partial\Omega_D^e, \tag{2}$$

where m_{el} is the number of elements in Ω_D.

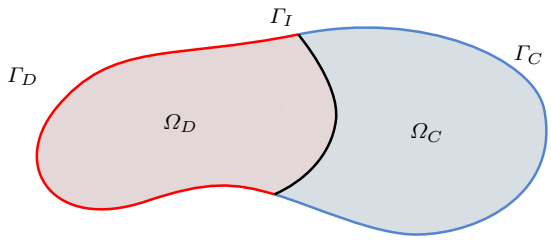

Fig. 1: Domain representation: HDG and CG discretizations are considered in Ω_D and Ω_C, respectively.

Let $\boldsymbol{w}$ and z be generic vector and scalar fields, respectively, defined over Ω. Their error norms are computed as follows,

$$\begin{aligned} ||e_{\boldsymbol{w}}||_{\mathcal{L}_2(\Omega)} &= \left[\int_\Omega (\boldsymbol{w}_{ex} - \boldsymbol{w}_{num}) \cdot (\boldsymbol{w}_{ex} - \boldsymbol{w}_{num}) \, \mathrm{d}\Omega\right]^{1/2}, \\ ||e_z||_{\mathcal{L}_2(\Omega)} &= \left[\int_\Omega (z_{ex} - z_{num})^2 \, \mathrm{d}\Omega\right]^{1/2}, \end{aligned} \tag{3}$$

where suffixes ex and num stand for exact and numerical values.

3 CG-HDG coupled formulation for the heat equation

This section presents suitable formulations for the solution of the heat equation coupling HDG discretization in Ω_D and CG discretization in Ω_C.

3.1 Governing equations

The heat equation in Ω_D and Ω_C, along with the transmission conditions on Γ_I, are

$$\boldsymbol{q}_D + (k_D \operatorname{grad} \theta_D) = \boldsymbol{0} \quad \text{in} \quad \Omega_D, \tag{4a}$$
$$\operatorname{div} \boldsymbol{q}_D = \bar{g}_D \quad \text{in} \quad \Omega_D, \tag{4b}$$
$$-\operatorname{div}\,(k_C \operatorname{grad} \theta_C) = \bar{g}_C \quad \text{in} \quad \Omega_C, \tag{4c}$$
$$\theta_D = \bar{\theta}_D \quad \text{on} \quad \Gamma_D, \tag{4d}$$
$$\theta_C = \bar{\theta}_C \quad \text{on} \quad \Gamma_C, \tag{4e}$$
$$\theta_D - \theta_C = 0 \quad \text{on} \quad \Gamma_I, \tag{4f}$$
$$\boldsymbol{q}_D \cdot \boldsymbol{n}_D - (k_C \operatorname{grad} \theta_C) \cdot \boldsymbol{n}_C = 0 \quad \text{on} \quad \Gamma_I, \tag{4g}$$

where θ_D and θ_C are the temperatures in Ω_D and Ω_C, respectively and $\boldsymbol{q}_D$ is the independently approximated flux in Ω_D. Heat conductivity coefficients are denoted by k_D, k_C, heat generations per unit volume are given by $\bar{g}_D$, $\bar{g}_C$, where the subscripts D and C denote that quantities are defined in Ω_D and Ω_C,

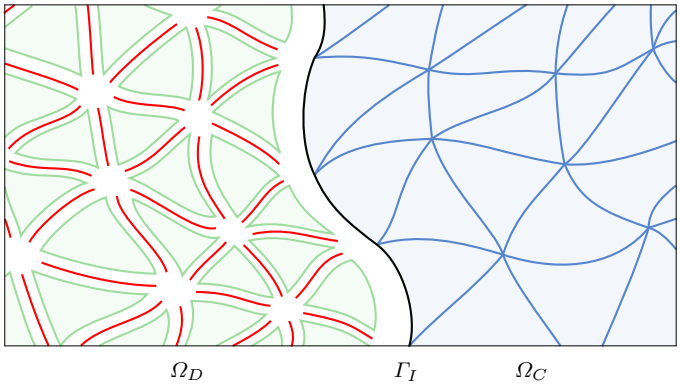

Fig. 2: Representation of a computational mesh for coupled discretization. *Green* triangles represent the HDG local elemental variables while the *red* edges correspond to HDG trace variable. CG mesh is represented in *blue* and Γ_I is represented in *black*.

respectively. Unit normal vectors on Γ_I, $\boldsymbol{n}_D$ and $\boldsymbol{n}_C$, are outward vectors to Ω_D and Ω_C, respectively, which satisfy $\boldsymbol{n}_D = -\boldsymbol{n}_C$. Dirichlet boundary conditions are prescribed with values $\bar{\theta}_D$ and $\bar{\theta}_C$ for both sub-domains on the exterior boundaries to simplify the presentation. The extension of the formulation to problems including Neumann boundary conditions on the exterior boundary is straightforward following the usual procedure for HDG or CG formulations.

Equation (4f) represents the continuity of θ, whereas (4g) states the equilibrium of the normal flux across the interface.

3.2 Weak formulation of the CG-HDG coupled problem

As shown in fig. 2, in Ω_C the temperature field, θ_C, is approximated with a continuous space on the mesh represented in blue, while in the HDG domain, Ω_D, the elemental variables θ_D and $\boldsymbol{q}_D$ are approximated within each element represented in green and a new independently approximated trace variable, $\hat{\theta}_D$, is defined along the red edges (mesh skeleton).

The CG weak form of the heat equation in Ω_C is,

$$(\operatorname{grad}\delta\theta_C, k_C \operatorname{grad}\theta_C)_{\Omega_C} - \langle \delta\theta_C, k_C (\operatorname{grad}\theta_C \cdot \boldsymbol{n}_C)\rangle_{\Gamma_I} - (\delta\theta_C, \bar{g}_C)_{\Omega_C} = 0, \quad (5)$$

where $\delta\theta_C = 0$ on Γ_C. Equation (5) is obtained after multiplying equation (4c) with $\delta\theta_C$ and performing integration by parts.

For the HDG domain, Ω_D, the discrete problem is expressed as element-by-element local problems and the so-called global problem (see [11] for more details). Note that the only difference of equations (8) with the standard HDG local problem is that the Dirichlet data, that is imposed in weak is

$$\theta_D = \begin{cases} \hat{\theta}_D & \text{on } \partial\Omega_D^e \backslash \Gamma_I, \\ \theta_C & \text{on } \partial\Omega_D^e \cap \Gamma_I. \end{cases} \quad (6)$$

For the elements along the interface, no trace variables are considered, as illustrated in fig. 2. For elements in the interior of Ω_D, the local problem is the standard one, with a weak imposition of $\theta_D = \hat{\theta}_D$ on $\partial\Omega_D^e$. The Dirichlet boundary condition (6) ensures the weak continuity of the temperature, *i.e.*, the transmission condition (4f) on Γ_I. The HDG numerical normal flux, $\hat{\boldsymbol{q}}_D \cdot \boldsymbol{n}$, is defined as,

$$\hat{\boldsymbol{q}}_D \cdot \boldsymbol{n} = \begin{cases} \boldsymbol{q}_D \cdot \boldsymbol{n} + \tau(\theta_D - \hat{\theta}_D) & \text{on } \partial\Omega_D^e \backslash \Gamma_I, \\ \boldsymbol{q}_D \cdot \boldsymbol{n}_D + \tau(\theta_D - \theta_C) & \text{on } \partial\Omega_D^e \cap \Gamma_I. \end{cases} \tag{7}$$

Therefore, the *local problem* in each element can be written as,

$$\begin{aligned} (\delta\theta_D, \operatorname{div} \boldsymbol{q}_D)_{\Omega_D^e} + \left\langle \delta\theta_D, \tau(\theta_D - \hat{\theta}_D) \right\rangle_{\partial\Omega_D^e \backslash \Gamma_I} \\ + \langle \delta\theta_D, \tau(\theta_D - \theta_C) \rangle_{\partial\Omega_D^e \cap \Gamma_I} - (\delta\theta_D, \bar{g}_D)_{\Omega_D^e} = 0, \\ \left(\delta\boldsymbol{q}_D, k_D^{-1}\boldsymbol{q}_D\right)_{\Omega_D^e} - (\operatorname{div} \delta\boldsymbol{q}_D, \theta_D)_{\Omega_D^e} + \left\langle \delta\boldsymbol{q}_D \cdot \boldsymbol{n}, \hat{\theta}_D \right\rangle_{\partial\Omega_D^e \backslash \Gamma_I} \\ + \langle \delta\boldsymbol{q}_D \cdot \boldsymbol{n}_D, \theta_C \rangle_{\partial\Omega_D^e \cap \Gamma_I} = 0, \end{aligned} \tag{8}$$

where $\hat{\theta}_D$ is an independently approximated trace variable along the mesh skeleton, Γ, which is represented in red in fig. 2, and τ is a parameter of order $\mathcal{O}(k_D)$. Parameter τ has an important effect on stability, accuracy and convergence properties of the HDG method (see [10,36]). As usual in HDG, the local problem can be solved element-by-element to express θ_D and $\boldsymbol{q}_D$ in terms of $\hat{\theta}_D$ and, in the present case, θ_C as well.

The *global problem* in Ω_D is the usual HDG global problem, which can be presented as

$$\sum_{e=1}^{m_{el}} \left\langle \delta\hat{\theta}_D, \hat{\boldsymbol{q}}_D \cdot \boldsymbol{n} \right\rangle_{\partial\Omega_D^e \backslash \Gamma_I} = 0, \tag{9a}$$

$$\hat{\theta}_D = \mathbb{P}_2(\bar{\theta}_D) \quad \text{on } \Gamma_D, \tag{9b}$$

where $\delta\hat{\theta}_D = 0$ on Γ_D, $\mathbb{P}_2(\bar{\theta}_D)$ is the $\mathcal{L}_2$ projection of the Dirichlet data into the approximation space on Γ_D.

Essentially, the global problem (9a) states the so-called conservativity condition, *i.e*, the weak continuity of the normal flux across all the interior faces of the mesh in Ω_D. The continuity of the fluxes on the interface, Γ_I, *i.e.*, equation (4g), is imposed between the numerical normal flux of HDG, $\hat{\boldsymbol{q}}_D \cdot \boldsymbol{n}_D$, which is defined in equation (7) and the flux on the interface from Ω_C, which is $-k_C \operatorname{grad} \theta_C \cdot \boldsymbol{n}_C$, leading to,

$$-\langle \delta\theta_C, \boldsymbol{q}_D \cdot \boldsymbol{n}_D + \tau(\theta_D - \theta_C) \rangle_{\Gamma_I} + \langle \delta\theta_C, k_C \operatorname{grad} \theta_C \cdot \boldsymbol{n}_C \rangle_{\Gamma_I} = 0. \tag{10}$$

By summing equation (10) to the weak form of CG in Ω_C (5), and using the weak formulation of HDG, (8) and (9), in Ω_D, the coupled discrete problem is

obtained: find $(\boldsymbol{q}_D, \theta_D, \hat{\theta}_D, \theta_C) \in \left[\mathcal{V}^h\right]^d \times \mathcal{V}^h \times \Lambda^h \times \mathcal{V}_c^h$ such that $\hat{\theta}_D = \mathbb{P}_2(\bar{\theta}_D)$ on Γ_D, $\theta_C = \Pi^h(\bar{\theta}_C)$ on Γ_C and

$$\begin{aligned}(\delta\theta_D, \operatorname{div} \boldsymbol{q}_D)_{\Omega_D^e} + \left\langle \delta\theta_D, \tau(\theta_D - \hat{\theta}_D)\right\rangle_{\partial\Omega_D^e\setminus\Gamma_I} \\ + \langle \delta\theta_D, \tau(\theta_D - \theta_C)\rangle_{\partial\Omega_D^e\cap\Gamma_I} - (\delta\theta_D, \bar{g}_D)_{\Omega_D^e} = 0, \\ \left(\delta\boldsymbol{q}_D, k_D^{-1}\boldsymbol{q}_D\right)_{\Omega_D^e} - (\operatorname{div}\delta\boldsymbol{q}_D, \theta_D)_{\Omega_D^e} + \left\langle \delta\boldsymbol{q}_D\cdot\boldsymbol{n}, \hat{\theta}_D\right\rangle_{\partial\Omega_D^e\setminus\Gamma_I} \\ + \langle \delta\boldsymbol{q}_D\cdot\boldsymbol{n}_D, \theta_C\rangle_{\partial\Omega_D^e\cap\Gamma_I} = 0,\end{aligned} \tag{11a}$$

for $e = 1, \ldots, m_{el}$ and,

$$\sum_{e=1}^{m_{el}} \left\langle \delta\hat{\theta}_D, \left(\boldsymbol{q}_D\cdot\boldsymbol{n} + \tau(\theta_D - \hat{\theta}_D)\right)\right\rangle_{\partial\Omega_D^e\setminus\Gamma_I} = 0, \tag{11b}$$

$$\begin{aligned}(\operatorname{grad}\delta\theta_C, k_C \operatorname{grad}\theta_C)_{\Omega_C} - \langle \delta\theta_C, \boldsymbol{q}_D\cdot\boldsymbol{n}_D + \tau(\theta_D - \theta_C)\rangle_{\Gamma_I} \\ - (\delta\theta_C, \bar{g}_C)_{\Omega_C} = 0.\end{aligned} \tag{11c}$$

for all $(\delta\boldsymbol{q}_D, \delta\theta_D, \delta\hat{\theta}_D, \delta\theta_C) \in \left[\mathcal{V}^h\right]^d \times \mathcal{V}^h \times \Lambda^h \times \mathcal{V}_c^h$ such that $\delta\hat{\theta}_D = 0$ on Γ_D and $\delta\theta_C = 0$ on Γ_C, where the discrete spaces are defined as

$$\begin{aligned}\mathcal{V}^h &:= \left\{v \in \mathcal{L}_2(\Omega_D) \;:\; v|_{\Omega^e} \in \mathcal{P}_k(\Omega^e), \forall\, \Omega^e \subset \Omega_D\right\}, \\ \Lambda^h &:= \left\{\hat{v} \in \mathcal{L}_2(\Gamma\setminus\Gamma_I) \;:\; \hat{v}|_{\Gamma_i} \in \mathcal{P}_k(\Gamma_i), \forall\, \Gamma_i \subset \Gamma\right\}, \\ \mathcal{V}_c^h &:= \left\{v \in \mathcal{H}^1(\Omega_C) \;:\; v|_{\Omega^e} \in \mathcal{P}_r(\Omega^e), \forall\, \Omega^e \subset \Omega_C\right\}.\end{aligned} \tag{12}$$

As usual in HDG, the spaces for approximation in Ω_D, $\mathcal{V}^h$ and Λ^h, consider polynomials of the same degree k for all variables. Numerical tests in section 3.5 show that the HDG super-convergence cannot be retained by the coupling with the CG approximation of same degree, $r = k$. However, as expected, convergence rates of order $k+2$ for the solution, and of order $k+1$ for the flux, are obtained when higher degree $r = k+1$ is considered for the CG approximation space $\mathcal{V}_c^h$.

The discretization of the system of equations in (11) gives rise to a matrix equation of the form

$$\left[\begin{array}{cc:cc} \mathbf{A}_{\hat{\theta}\hat{\theta}} & \mathbf{0} & \mathbf{A}_{\hat{\theta}\theta} & \mathbf{A}_{\hat{\theta}q} \\ \mathbf{0} & \mathbf{K}_{\theta\theta} & \mathbf{B}_{\theta\theta}^T & \mathbf{B}_{\theta q} \\ \hdashline \mathbf{A}_{\theta\hat{\theta}} & \mathbf{B}_{\theta\theta} & \mathbf{A}_{\theta\theta} & \mathbf{A}_{\theta q} \\ \mathbf{A}_{q\hat{\theta}} & \mathbf{B}_{q\theta} & \mathbf{A}_{q\theta} & \mathbf{A}_{qq} \end{array}\right] \left\{\begin{array}{c} \hat{\boldsymbol{\theta}}_D \\ \boldsymbol{\theta}_C \\ \hdashline \boldsymbol{\theta}_D \\ \mathbf{q}_D \end{array}\right\} = \left\{\begin{array}{c} \mathbf{0} \\ \bar{\mathbf{g}}_C \\ \hdashline \bar{\mathbf{g}}_D \\ \mathbf{0} \end{array}\right\}. \tag{13}$$

The column vectors $\boldsymbol{\theta}_D, \mathbf{q}_D, \hat{\boldsymbol{\theta}}_D$ and $\boldsymbol{\theta}_C$ contain the DOFs associated to $\theta_D, \boldsymbol{q}_D, \hat{\theta}_D$ and θ_C, respectively. Static condensation is assumed for the CG discretization, expressing the nodal values of interior nodes of the element in terms of the nodal values on the edges. The elemental matrices in equation (13) are defined in the appendix.

As it is well explained in the literature, one of the attractive features of HDG is being able to express the local variables, $\boldsymbol{\theta}_D$ and $\mathbf{q}_D$, in terms of the

trace variable $\hat{\boldsymbol{\theta}}_D$. This is done by using static condensation technique applied in an element-by-element fashion (see, for instance [44]). In the present case, $\hat{\boldsymbol{\theta}}_D$ and $\boldsymbol{\theta}_C$ are coupled at the interface and hence, the local variables, $\boldsymbol{\theta}_D$ and $\mathbf{q}_D$, in the HDG domain Ω_D are expressed in terms of $\hat{\boldsymbol{\theta}}_D$ and $\boldsymbol{\theta}_C$. Therefore, system (13) can be expressed as follows,

$$\begin{Bmatrix} \boldsymbol{\theta}_D \\ \mathbf{q}_D \end{Bmatrix} = \begin{bmatrix} \mathbf{A}_{\theta\theta} & \mathbf{A}_{\theta q} \\ \mathbf{A}_{q\theta} & \mathbf{A}_{qq} \end{bmatrix}^{-1} \left(\begin{Bmatrix} \bar{\mathbf{g}}_D \\ \mathbf{0} \end{Bmatrix} - \begin{bmatrix} \mathbf{A}_{\theta\hat{\theta}} & \mathbf{B}_{\theta\theta} \\ \mathbf{A}_{q\hat{\theta}} & \mathbf{B}_{q\theta} \end{bmatrix} \begin{Bmatrix} \hat{\boldsymbol{\theta}}_D \\ \boldsymbol{\theta}_C \end{Bmatrix} \right), \tag{14a}$$

$$\begin{bmatrix} \mathbf{A}_{\hat{\theta}\theta} & \mathbf{A}_{\hat{\theta}q} \\ \mathbf{B}^T_{\theta\theta} & \mathbf{B}_{\theta q} \end{bmatrix} \begin{Bmatrix} \boldsymbol{\theta}_D \\ \mathbf{q}_D \end{Bmatrix} + \begin{bmatrix} \mathbf{A}_{\hat{\theta}\hat{\theta}} & \mathbf{0} \\ \mathbf{0} & \mathbf{K}_{\theta\theta} \end{bmatrix} \begin{Bmatrix} \hat{\boldsymbol{\theta}}_D \\ \boldsymbol{\theta}_C \end{Bmatrix} = \begin{Bmatrix} \mathbf{0} \\ \bar{\mathbf{g}}_C \end{Bmatrix}. \tag{14b}$$

Equation (14a) is the so-called HDG local solver, which can be computed element-wise owing to the fact that the equations corresponding to the local problem of an element do not involve elemental variables of other elements *i.e.,* the inverted matrix is block diagonal. By replacing equation (14a) in (14b), $\boldsymbol{\theta}_D$ and $\mathbf{q}_D$ are eliminated resulting in a system with unknowns only in $\hat{\boldsymbol{\theta}}_D$ and $\boldsymbol{\theta}_C$:

$$\begin{bmatrix} \mathbf{K}_{DD} & \mathbf{K}_{DC} \\ \mathbf{K}_{CD} & \mathbf{K}_{CC} \end{bmatrix} \begin{Bmatrix} \hat{\boldsymbol{\theta}}_D \\ \boldsymbol{\theta}_C \end{Bmatrix} = \begin{Bmatrix} \mathbf{f}_D \\ \mathbf{f}_C \end{Bmatrix}, \tag{15}$$

where

$$\begin{bmatrix} \mathbf{K}_{DD} & \mathbf{K}_{DC} \\ \mathbf{K}_{CD} & \mathbf{K}_{CC} \end{bmatrix} = \begin{bmatrix} \mathbf{A}_{\hat{\theta}\hat{\theta}} & \mathbf{0} \\ \mathbf{0} & \mathbf{K}_{\theta\theta} \end{bmatrix} - \begin{bmatrix} \mathbf{A}_{\hat{\theta}\theta} & \mathbf{A}_{\hat{\theta}q} \\ \mathbf{B}^T_{\theta\theta} & \mathbf{B}_{\theta q} \end{bmatrix} \begin{bmatrix} \mathbf{A}_{\theta\theta} & \mathbf{A}_{\theta q} \\ \mathbf{A}_{q\theta} & \mathbf{A}_{qq} \end{bmatrix}^{-1} \begin{bmatrix} \mathbf{A}_{\theta\hat{\theta}} & \mathbf{B}_{\theta\theta} \\ \mathbf{A}_{q\hat{\theta}} & \mathbf{B}_{q\theta} \end{bmatrix}, \tag{16a}$$

$$\begin{Bmatrix} \mathbf{f}_D \\ \mathbf{f}_C \end{Bmatrix} = \begin{Bmatrix} \mathbf{0} \\ \bar{\mathbf{g}}_C \end{Bmatrix} - \begin{bmatrix} \mathbf{A}_{\hat{\theta}\theta} & \mathbf{A}_{\hat{\theta}q} \\ \mathbf{B}^T_{\theta\theta} & \mathbf{B}_{\theta q} \end{bmatrix} \begin{bmatrix} \mathbf{A}_{\theta\theta} & \mathbf{A}_{\theta q} \\ \mathbf{A}_{q\theta} & \mathbf{A}_{qq} \end{bmatrix}^{-1} \begin{Bmatrix} \bar{\mathbf{g}}_D \\ \mathbf{0} \end{Bmatrix}. \tag{16b}$$

After solving the system in (15) for $\hat{\boldsymbol{\theta}}_D$ and $\boldsymbol{\theta}_C$, the HDG elemental local variables, $\boldsymbol{\theta}_D$ and $\mathbf{q}_D$, and the CG nodal values of the interior nodes can be computed by using (14a), and the CG static condensation.

3.3 Alternative CG-HDG coupled formulation with a projection operator on the interface

The coupled formulation presented earlier considers the standard HDG local problem for the elements that do not share the interface, $\partial\Omega^e_D \cap \Gamma_I = \emptyset$, and a non-standard HDG local problem imposing (6) in weak form for elements along the interface, $\partial\Omega^e_D \cap \Gamma_I \neq \emptyset$. In terms of implementation, additional matrices, $\mathbf{B}_{\theta\theta}$ and $\mathbf{B}_{\theta q}$, in the elements along the interface boundary Γ_I are needed for the non-standard HDG local solver. An alternative coupling formulation is proposed in this section to keep the implementation changes to minimum in any existing HDG and CG codes. The main idea in this formulation is to

use a projection to satisfy the transmission conditions. This formulation only requires the standard elemental matrices from HDG (after static condensation of local variables into trace variable) and CG domains, and a projection operation is used on the HDG elemental matrices before assembling into the global system. This requires minimal changes to the existing codes and it is noticed that, in the numerical results, this implementation gives practically the same results as the earlier one with same convergence rates.

In this case, the Dirichlet boundary conditions for the local problem are defined as follows,

$$\theta_D = \begin{cases} \hat{\theta}_D & \text{on } \partial\Omega_D^e \backslash \Gamma_I, \\ \mathbb{P}_2(\theta_C) & \text{on } \partial\Omega_D^e \cap \Gamma_I, \end{cases} \tag{17}$$

where in equation (17) the operator $\mathbb{P}_2$ stands for the $\mathcal{L}_2$ projection from the CG space $\mathcal{V}_c^h$ to the HDG space $\mathcal{V}^h$. Hence, the trace is set to the projection of the CG solution on the faces along the interface, *i.e.*, $\hat{\theta}_D = \mathbb{P}_2(\theta_C)$ on $\partial\Omega_D^e \cap \Gamma_I$. Consequently, the numerical normal flux is defined as,

$$\hat{\boldsymbol{q}}_D \cdot \boldsymbol{n} = \begin{cases} \boldsymbol{q}_D \cdot \boldsymbol{n} + \tau(\theta_D - \hat{\theta}_D) & \text{on } \partial\Omega_D^e \backslash \Gamma_I, \\ \boldsymbol{q}_D \cdot \boldsymbol{n}_D + \tau(\theta_D - \mathbb{P}_2(\theta_C)) & \text{on } \partial\Omega_D^e \cap \Gamma_I. \end{cases} \tag{18}$$

The jump of fluxes along the interface is weighted with $\mathbb{P}_2\left(\delta\theta_C\right)$ leading to,

$$-\left\langle \mathbb{P}_2\left(\delta\theta_C\right), \boldsymbol{q}_D \cdot \boldsymbol{n}_D + \tau\left(\theta_D - \mathbb{P}_2\left(\theta_C\right)\right)\right\rangle_{\Gamma_I} + \left\langle \mathbb{P}_2\left(\delta\theta_C\right), k_C \operatorname{grad}\theta_C \cdot \boldsymbol{n}_C\right\rangle_{\Gamma_I} = 0. \tag{19}$$

Using (17) and (19), the weak formulation of the coupled discrete problem becomes: find $(\boldsymbol{q}_D, \theta_D, \hat{\theta}_D, \theta_C) \in \left[\mathcal{V}^h\right]^d \times \mathcal{V}^h \times \Lambda^h \times \mathcal{V}_c^h$ such that $\hat{\theta}_D = \mathbb{P}_2(\bar{\theta}_D)$ on Γ_D, $\theta_C = \Pi^h(\bar{\theta}_C)$ on Γ_C and

$$\begin{aligned} &\left(\delta\theta_D, \operatorname{div}\boldsymbol{q}_D\right)_{\Omega_D^e} + \left\langle \delta\theta_D, \tau(\theta_D - \hat{\theta}_D)\right\rangle_{\partial\Omega_D^e \backslash \Gamma_I} \\ &\qquad + \left\langle \delta\theta_D, \tau(\theta_D - \mathbb{P}_2\left(\theta_C\right))\right\rangle_{\partial\Omega_D^e \cap \Gamma_I} - \left(\delta\theta_D, \bar{g}_D\right)_{\Omega_D^e} = 0, \\ &\left(\delta\boldsymbol{q}_D, k_D^{-1}\boldsymbol{q}_D\right)_{\Omega_D^e} - \left(\operatorname{div}\delta\boldsymbol{q}_D, \theta_D\right)_{\Omega_D^e} + \left\langle \delta\boldsymbol{q}_D \cdot \boldsymbol{n}, \hat{\theta}_D\right\rangle_{\partial\Omega_D^e \backslash \Gamma_I} \\ &\qquad + \left\langle \delta\boldsymbol{q}_D \cdot \boldsymbol{n}_D, \mathbb{P}_2\left(\theta_C\right)\right\rangle_{\partial\Omega_D^e \cap \Gamma_I} = 0, \end{aligned} \tag{20a}$$

for $e = 1, \ldots, m_{el}$ and,

$$\sum_{e=1}^{m_{el}} \left\langle \delta\hat{\theta}_D, \left(\boldsymbol{q}_D \cdot \boldsymbol{n} + \tau(\theta_D - \hat{\theta}_D)\right)\right\rangle_{\partial\Omega_D^e \backslash \Gamma_I} = 0, \tag{20b}$$

$$\begin{aligned} &\left(\operatorname{grad}\delta\theta_C, k_C \operatorname{grad}\theta_C\right)_{\Omega_C} - \left\langle \mathbb{P}_2\left(\delta\theta_C\right), \boldsymbol{q}_D \cdot \boldsymbol{n}_D + \tau\left(\theta_D - \mathbb{P}_2\left(\theta_C\right)\right)\right\rangle_{\Gamma_I} \\ &\qquad + \left\langle \left(\mathbb{P}_2\left(\delta\theta_C\right) - \delta\theta_C\right), k_C \operatorname{grad}\theta_C \cdot \boldsymbol{n}_C\right\rangle_{\Gamma_I} - \left(\delta\theta_C, \bar{g}_C\right)_{\Omega_C} = 0. \end{aligned} \tag{20c}$$

for all $(\delta\boldsymbol{q}_D, \delta\theta_D, \delta\hat{\theta}_D, \delta\theta_C) \in \left[\mathcal{V}^h\right]^d \times \mathcal{V}^h \times \Lambda^h \times \mathcal{V}_c^h$ such that $\delta\hat{\theta}_D = 0$ on Γ_D and $\delta\theta_C = 0$ on Γ_C.

The weak form in equations (20) is similar to one presented earlier in equations (11) except for two major differences. First, θ_C is now replaced by its projection, $\mathbb{P}_2(\theta_C)$, in the HDG local problems (20a), and, second, an additional term $\langle(\mathbb{P}_2\left(\delta\theta_C\right) - \delta\theta_C), k_C \operatorname{grad}\theta_C \cdot \boldsymbol{n}_C\rangle_{\Gamma_I}$ appears in the last equation (20c). The implementation of this new term maybe cumbersome, because it requires the computation of the gradient of the CG elemental basis functions on the integration points on the interface. However, $\mathbb{P}_2\left(\delta\theta_C\right) - \delta\theta_C = \mathcal{O}(h^{k+1})$, where h is the mesh size and k is degree of approximation, and therefore, this term can be safely neglected in the discrete problem without losing neither the convergence nor the accuracy of the solution.

This formulation does not require the computation of the new matrices that arise in (11), namely $\mathbf{B}_{\theta\theta}$ and $\mathbf{B}_{\theta q}$. The projection operation can be done in an element-by-element basis on the HDG elemental matrices for the elements along the interface boundary. For the sake of simplifying the presentation the nodal values of the CG approximation, $\boldsymbol{\theta}_C$, are split into values for nodes on the interface, $\boldsymbol{\theta}_C^I$, and the remaining CG nodal values, $\boldsymbol{\theta}_C^i$. The global stiffness matrix can be then represented as,

$$\begin{bmatrix} \mathbf{K}_{DD} & \mathbf{K}_{DI}\mathbf{P} & \mathbf{0} \\ \mathbf{P}^T\mathbf{K}_{ID} & \mathbf{P}^T\mathbf{K}_{II}^D\mathbf{P} + \mathbf{K}_{II}^C & \mathbf{K}_{IC} \\ \mathbf{0} & \mathbf{K}_{CI} & \mathbf{K}_{CC} \end{bmatrix} \begin{Bmatrix} \hat{\boldsymbol{\theta}}_D \\ \boldsymbol{\theta}_C^I \\ \boldsymbol{\theta}_C^i \end{Bmatrix} = \begin{Bmatrix} \mathbf{f}_D \\ \mathbf{P}^T\mathbf{f}_I^D + \mathbf{f}_I^C \\ \mathbf{f}_C \end{Bmatrix}, \tag{21}$$

where in equation (21), $\mathbf{P}$ is the assembly of projection matrices on all the faces along the interface. This implementation can be easily plugged into any existing HDG solver for heat equation.

Both coupled formulations (11) and (20) have been implemented and the comparison of the numerical results inferred that both are practically identical. In some tests, the first proposed formulation (11) gave slightly smaller errors. The difference might be due to neglecting the term $\mathbb{P}_2\left(\delta\theta_C\right) - \delta\theta_C$ in the last formulation (20). However, the difference in the errors — even for the coarsest mesh — is negligible and, hence, in all the results presented in this work, the formulation with projection (20) is used neglecting the term $\mathbb{P}_2\left(\delta\theta_C\right) - \delta\theta_C$.

3.4 Implementation details

In all the results presented in the current work the shape functions that are used to approximate the variables inside each element are generated using Fekete nodal distributions [46] for triangular elements and Gauss–Lobatto points [1, p. 888] in the case of quadrilateral elements. The shape functions are computed using Jacobi polynomials [23]. All the meshes are generated using EZ4U [42,43,29], which is a high order mesh generator, and Gmsh [20] is used to post process the results.

The non-linear system of equations is solved using full Newton–Raphson method. Relative incremental and residual norms are used as convergence criteria with a tolerance of 10^{-12}.

An in-house code is implemented in FORTRAN. Harwell Subroutine Library (HSL) [25] routine MA57d and MA41d [4] are used for solving symmetric and unsymmetric systems, respectively. Both solvers use Approximate Minimum Degree (AMD) [3] reordering algorithm to reorder the linear system of equations. MC75d [47] is used to estimate the condition number of the tangent stiffness matrices, $\kappa(\mathbf{A})$.

All tests were performed on machine equipped with 24 Intel(R) Xeon(R) E5-2620 v2 2.10-2.60 GHz processors and 64 GB of RAM running OpenSUSE 13.1 (x86_64) using a serial implementation. The code was compiled using gfortran 4.8.1.

3.5 Convergence

In this section, the convergence results of the coupled CG-HDG formulation for the heat equation are presented. A square domain, $\Omega := [0,1]^2$ is considered with the analytical solution,

$$\theta = 1 + \cos(\pi x_1)\cos(\pi x_2). \tag{22}$$

Dirichlet boundary conditions are prescribed on all the exterior boundary.

The domain is divided into two halves in vertical direction. The domain corresponding to HDG is $\Omega_D := [0, 0.5] \times [0, 1]$, the CG domain is $\Omega_C := [0.5, 1] \times [0, 1]$, and the interface, Γ_I, is $x_1 = 0.5$. A suitable body force is computed from the heat equation with the considered analytical solution for both domains, with the conductivity constants, $k_C = k_D = 1$.

Meshes are obtained by splitting a regular $n \times n$ Cartesian grid into $2n^2$ triangles, which gives an uniform mesh element size, $h = 1/n$. The results presented here consider a parameter of $\tau = 1$ on all faces of each element in HDG domain, Ω_D.

Figure 3 shows the convergence for the coupled formulation with same degree for CG and HDG, with $k = 1-8$ and element size, $h = 0.5/\{1, 2, 4, 8, 16\}$. The error in θ is measured by using $\mathcal{L}_2$ norm of errors of the post-processed solution, θ^*_D, in Ω_D, and CG solution, θ_C, in Ω_C. Similarly, error in $\operatorname{grad}\theta$ is computed using $\mathcal{L}_2$ norm of error in $\boldsymbol{q}_D$ in Ω_D and error in $\operatorname{grad}\theta_C$ in Ω_C, that is,

$$\begin{aligned} \|e_\theta\|_{\mathcal{L}_2(\Omega)} &= \sqrt{\left\|e_{\theta^*_D}\right\|^2_{\mathcal{L}_2(\Omega_D)} + \|e_{\theta_C}\|^2_{\mathcal{L}_2(\Omega_C)}}, \\ \|e_{\operatorname{grad}\theta}\|_{\mathcal{L}_2(\Omega)} &= \sqrt{\left\|e_{\boldsymbol{q}_D}\right\|^2_{\mathcal{L}_2(\Omega_D)} + \|e_{\operatorname{grad}\theta_C}\|^2_{\mathcal{L}_2(\Omega_C)}}. \end{aligned} \tag{23}$$

When the degree of approximation k is used for both HDG and CG domains, even though HDG has superior convergence properties, errors in CG domain dominates for both θ and $\operatorname{grad}\theta$. Hence, as shown in fig. 3a, the order of convergence of the coupled solution is $k+1$ for θ. Similarly, for $\operatorname{grad}\theta$, the order of convergence is k.

Figure 4 shows the convergence of θ^*_D and $\boldsymbol{q}_D$ in Ω_D for the coupled CG(P_k)-HDG(P_k) model. Sub-optimal convergence rates are observed in both

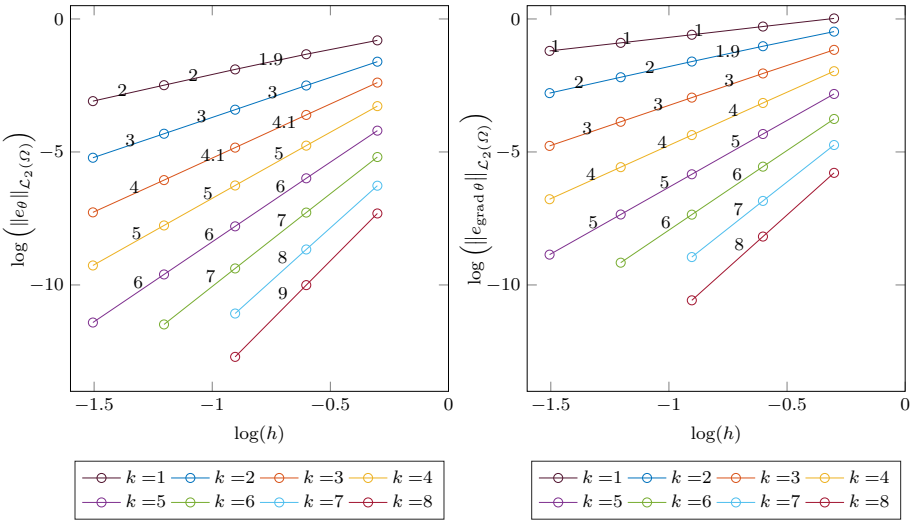

(a) θ. (b) grad θ.

Fig. 3: Coupled CG(P_k)-HDG(P_k): convergence plots in Ω.

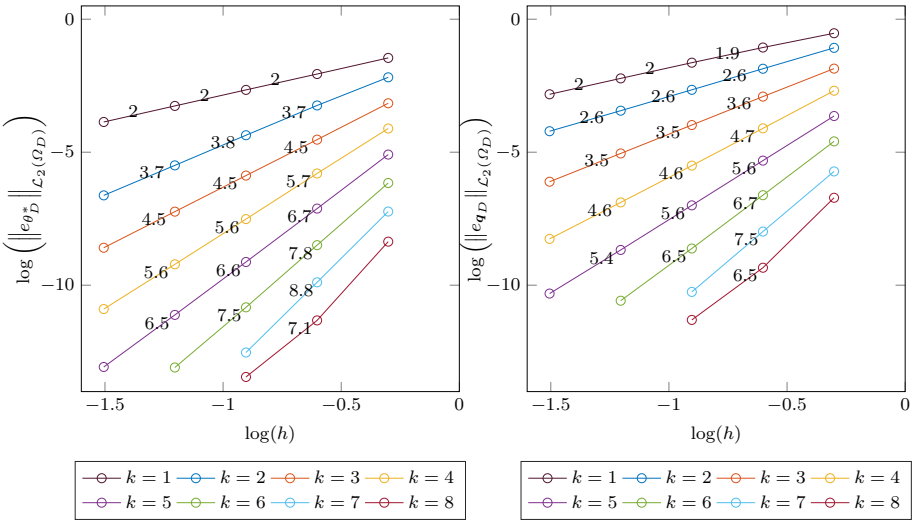

(a) θ_D^*. (b) $\boldsymbol{q}_D$.

Fig. 4: Coupled CG(P_k)-HDG(P_k): convergence plots in Ω_D.

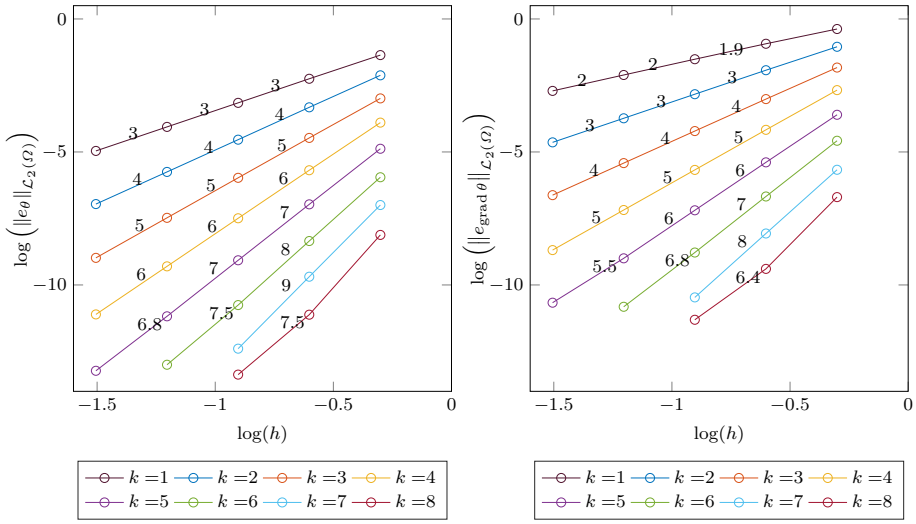

(a) θ. (b) grad θ.

Fig. 5: Coupled CG(P_{k+1})-HDG(P_k): convergence plots in Ω.

variables: for $k > 2$, θ_D^* converges with only $k + 1.5$ instead of $k + 2$, and $\boldsymbol{q}_D$ converges with order $k+0.5$ instead of $k+1$. HDG super-convergence requires a solution of order $k + 1$ for $\boldsymbol{q}_D$, and mean of θ_D that converges with order $k+2$ in each element in Ω_D. The elements in Ω_D that share the interface, Γ_I, do not possess the mentioned convergence rates because of the coupling with CG domain, Ω_C.

To address this shortcoming, higher degree of approximation is considered for the CG discretization. Figure 5a shows the convergence plots for a coupled approximation with degree k for HDG and degree $k + 1$ for CG. Optimal convergence rates of both methods are retained in this case. The post-processed solution of HDG with degree k has the same order of convergence, which is $k + 2$, as the CG solution with degree $k + 1$. Similarly, the flux $\boldsymbol{q}_D$ of HDG converges with same order as grad θ_C of CG, which is $k + 1$.

The same conclusions are drawn for quadrilateral elements as well and, hence, the results are omitted.

3.6 Influence of τ parameter on coupled formulation

This section presents the study of effect of parameter, τ, on the coupled formulation. Two different cases are considered in this study namely, single-face [9] and all-face [12] techniques. In all-face approach, τ is a positive value for all the edges of each element whereas, in single-face approach, τ is zero on all edges except an arbitrarily chosen edge of each element. The convergence results presented earlier use all-face approach. However, previous works [10, 22]

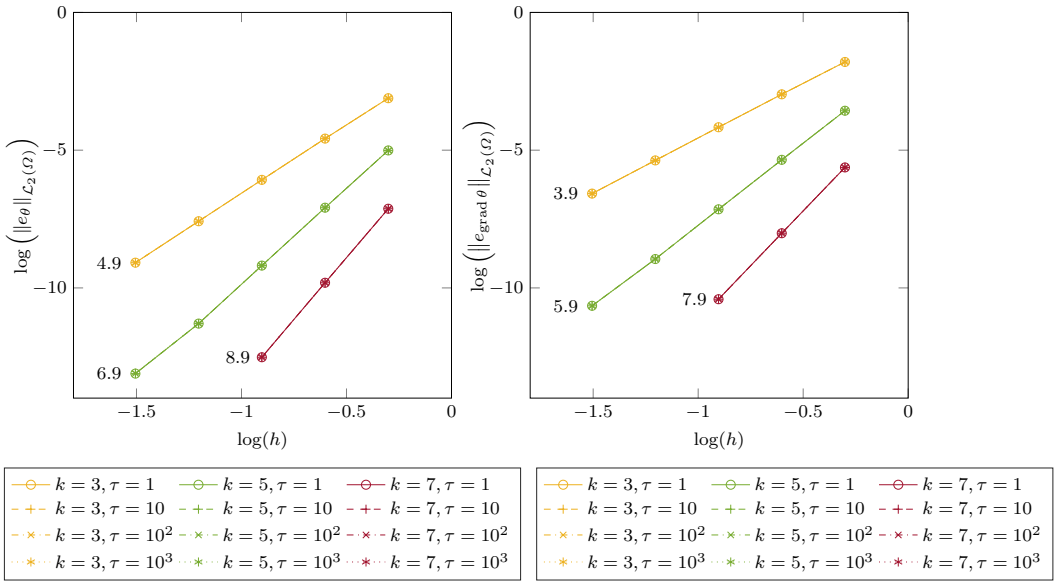

(a) θ. (b) grad θ.

Fig. 6: Coupled CG(P_{k+1})-HDG(P_k): convergence of $\mathcal{L}_2$ norm of θ and grad θ in Ω showing the influence of parameter, τ, on coupled solution for single-face approach.

conclude that the method is less sensitive to the choice of τ with the single-face definition, resulting in a more robust formulation than all-face approach in the case of second-order elliptic operators. Hence, both cases are investigated in the context of the present coupled formulation.

Figures 6 and 7 show the convergence of temperature and gradient of temperature for different values of τ, for single-face and all-face approach, respectively. The results are in agreement with the conclusions in [22]. In the case of single-face approach, the error values are practically the same for different values of τ. It can also be noticed that optimal rates of convergence are achieved for both temperature and gradient of temperature. It is worthy to note that it is possible to take $\tau = 0$ on all faces sharing the interface without loss of neither convergence nor accuracy in the single-face approach. However, in the case of all-face approach, as the parameter, τ, is increased, the optimal rate of convergence is lost. From fig. 7, it is clear that both temperature and gradient of temperature show sub-optimal convergence for τ significantly larger than 1, due to loss of optimal convergence in the HDG domain.

Even though stable and accurate solutions are obtained in all cases, it is therefore recommended to use single-face approach as it is less sensitive to the value of parameter τ.

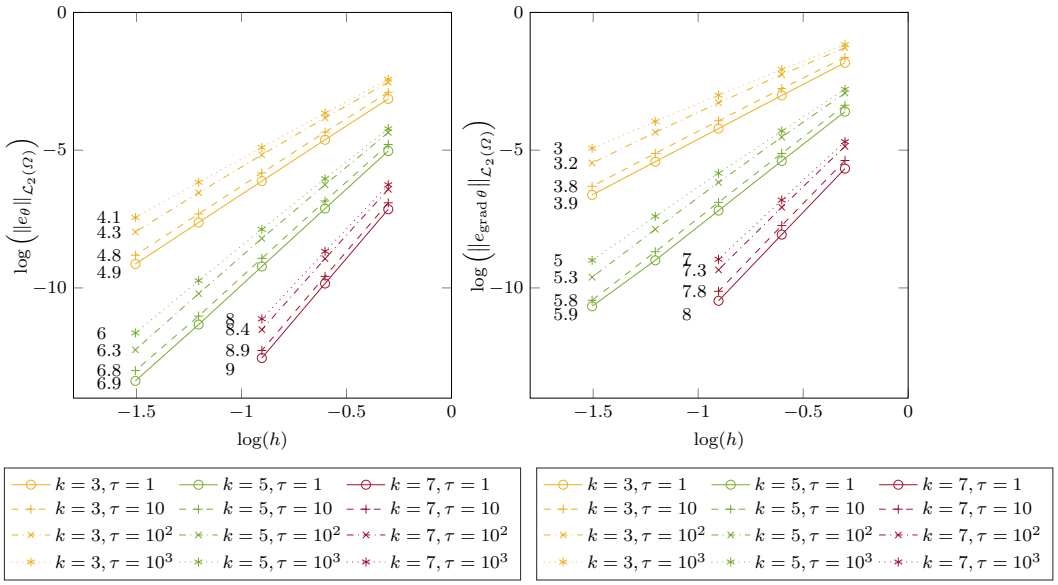

(a) θ. (b) $\mathrm{grad}\,\theta$.

Fig. 7: Coupled CG(P_{k+1})-HDG(P_k): convergence $\mathcal{L}_2$ norm of θ and $\mathrm{grad}\,\theta$ in Ω demonstrating the influence of parameter, τ, on coupled formulation for all-face approach.

4 HDG formulation for coupled Navier–Stokes/convection-diffusion equations

4.1 Governing equations

Let $\Omega = \Omega_D$ be the fluid domain with boundary $\partial\Omega$ divided into Dirichlet, $\partial\Omega_D$, and Neumann, $\partial\Omega_N$, boundaries. The steady state incompressible Navier–Stokes and convection-diffusion equations can be expressed as,

$$\begin{aligned}
\mathrm{div}\,(\boldsymbol{u}\otimes\boldsymbol{u}) - \mathrm{div}\,(-p\boldsymbol{I} + \nu\,\mathrm{grad}\,\boldsymbol{u}) &= \boldsymbol{f}\,(\theta) + \bar{\boldsymbol{s}} && \text{in} \quad \Omega,\\
\mathrm{div}\,\boldsymbol{u} &= 0 && \text{in} \quad \Omega,\\
\boldsymbol{u}\cdot(\mathrm{grad}\,\theta) - \mathrm{div}\,(\alpha\,\mathrm{grad}\,\theta) &= \bar{g} && \text{in} \quad \Omega,\\
\boldsymbol{u} &= \bar{\boldsymbol{u}} && \text{on} \quad \partial\Omega_D,\\
\theta &= \bar{\theta} && \text{on} \quad \partial\Omega_D,\\
(-p\boldsymbol{I} + \nu\,\mathrm{grad}\,\boldsymbol{u})\,\boldsymbol{n} &= \bar{\boldsymbol{t}} && \text{on} \quad \partial\Omega_N,\\
(-\alpha\,\mathrm{grad}\,\theta + \boldsymbol{u}\,\theta)\cdot\boldsymbol{n} &= \bar{q}_n && \text{on} \quad \partial\Omega_N,
\end{aligned} \tag{24}$$

where $\boldsymbol{u}$, θ and p are velocity, temperature and kinematic pressure, respectively. Material properties ν and α are kinematic viscosity and thermal diffusivity, respectively. $\boldsymbol{f}\,(\theta)$ is the body force, which is a function of temperature,

$\bar{\boldsymbol{s}}$ is an additional external body force acting on fluid and $\bar{g}$ is the volumetric heat generation. $\bar{\boldsymbol{u}}$ and $\bar{\theta}$ are the prescribed velocity and temperature on the Dirichlet boundary, $\partial\Omega_D$, and $\bar{\boldsymbol{t}}$ and $\bar{q}_n$ are the prescribed pseudo tractions and normal flux on the Neumann boundary, $\partial\Omega_N$.

As it is clear from the governing equations, this is a coupled system in $\boldsymbol{u}, p$ and θ. The convective term $\boldsymbol{u}\cdot(\operatorname{grad}\theta)$ in the convection-diffusion equation influences the temperature distribution and the body force $\boldsymbol{f}(\theta)$ in momentum equations governs the velocity of the fluid. Hence, a coupled system is established in both directions. In the present work, natural buoyancy flows are considered and Boussinesq approximation is used to compute the approximate body force, $\boldsymbol{f}(\theta)$, of Navier–Stokes equations. The artificial linear variation of density with temperature is expressed as,

$$\rho = \rho_0 \left(1 - \beta\left(\theta - \theta_0\right)\right), \tag{25}$$

where β is the thermal expansion coefficient and θ_0 is the reference temperature. The density is assumed to be constant to that of the reference state, ρ_0. The gravitational force due to the artificial variation of the density can be expressed as the following body force vector per unit of mass of the reference state

$$\boldsymbol{f}(\theta) = \frac{\boldsymbol{g}(\rho - \rho_0)}{\rho_0} = -\boldsymbol{g}\beta(\theta - \theta_0), \tag{26}$$

where $\boldsymbol{g}$ is the gravity acceleration vector. The important non-dimensional numbers that are used in the context of natural buoyancy flows are Rayleigh number (Ra) and Prandtl number (Pr), which are defined as,

$$Ra = \frac{g\beta L_{ref}^3 \Delta\theta}{\nu\alpha}, \quad Pr = \frac{\nu}{\alpha}, \quad \text{where} \quad \alpha = \frac{\kappa}{\rho_0 c_p}. \tag{27}$$

In equation (27), κ is heat conductivity, L_{ref} and $\Delta\theta$ are the characteristic length and temperature difference in the domain, respectively.

4.2 HDG formulation

Using notation, $\boldsymbol{L} = \operatorname{grad}\boldsymbol{u}$ and $\boldsymbol{q} = -\alpha\operatorname{grad}\theta$, the HDG formulation of the coupled Navier–Stokes (see [21]) and convection-diffusion (see [10]) equations is: find $(\boldsymbol{u}, p, \boldsymbol{L}, \theta, \boldsymbol{q}, \hat{\boldsymbol{u}}, \boldsymbol{\rho}, \hat{\theta}) \in [\mathcal{V}^h]^d \times \mathcal{V}^h \times [\mathcal{V}^h]^{d\times d} \times \mathcal{V}^h \times [\mathcal{V}^h]^d \times [\Lambda^h]^d \times \mathbb{R}^{n_{el}} \times \Lambda^h$ satisfying the *local problem* in every element Ω^e,

$$
\begin{aligned}
&(\delta \boldsymbol{L}, \boldsymbol{L})_{\Omega^e} + (\operatorname{div} \delta \boldsymbol{L}, \boldsymbol{u})_{\Omega^e} - \langle \delta \boldsymbol{L} \boldsymbol{n}, \hat{\boldsymbol{u}} \rangle_{\partial \Omega^e} = 0, \\
&- (\operatorname{grad} \delta \boldsymbol{u}, \boldsymbol{u} \otimes \boldsymbol{u})_{\Omega^e} + (\delta \boldsymbol{u}, \operatorname{div}\, (-\nu \boldsymbol{L} + p \boldsymbol{I}))_{\Omega^e} \\
&\quad + \langle \delta \boldsymbol{u}, (\hat{\boldsymbol{u}} \otimes \hat{\boldsymbol{u}})\, \boldsymbol{n} + \tau_u\, (\boldsymbol{u} - \hat{\boldsymbol{u}}) \rangle_{\partial \Omega^e} - (\delta \boldsymbol{u}, \boldsymbol{f}(\theta))_{\Omega^e} - (\delta \boldsymbol{u}, \bar{\boldsymbol{s}})_{\Omega^e} = 0, \\
&- (\operatorname{grad} \delta p, \boldsymbol{u})_{\Omega^e} + \langle \delta p, \hat{\boldsymbol{u}} \cdot \boldsymbol{n} \rangle_{\partial \Omega^e} = 0,
\end{aligned}
\tag{28a}
$$

$$
\frac{1}{|\partial \Omega^e|} \langle p, 1 \rangle_{\partial \Omega^e} = \rho_e, \tag{28b}
$$

$$
\begin{aligned}
&\left(\delta \boldsymbol{q}, \alpha^{-1} \boldsymbol{q}\right)_{\Omega^e} - (\operatorname{div} \delta \boldsymbol{q}, \theta)_{\Omega^e} + \langle \delta \boldsymbol{q} \cdot \boldsymbol{n}, \hat{\theta} \rangle_{\partial \Omega^e} = 0, \\
&(\delta \theta, \operatorname{div} \boldsymbol{q})_{\Omega^e} - (\operatorname{grad} \delta \theta, \boldsymbol{u} \theta)_{\Omega^e} + \langle \delta \theta, (\hat{\boldsymbol{u}} \cdot \boldsymbol{n} - \tau_\theta)\, , \hat{\theta} \rangle_{\partial \Omega^e} \\
&\qquad + \langle \delta \theta, \tau_\theta \theta \rangle_{\partial \Omega^e} - (\delta \theta, \bar{g})_{\Omega^e} = 0,
\end{aligned}
\tag{28c}
$$

for $e = 1, \ldots, m_{el}$, and the *global problem*

$$
\begin{aligned}
&\sum_{e=1}^{m_{el}} \langle \delta \hat{\boldsymbol{u}}, (-p \boldsymbol{I} + \nu \boldsymbol{L})\, \boldsymbol{n} + \tau_u\, (\hat{\boldsymbol{u}} - \boldsymbol{u}) \rangle_{\partial \Omega^e} = \langle \delta \hat{\boldsymbol{u}}, \bar{\boldsymbol{t}} \rangle_{\partial \Omega_N}\, , \\
&\langle \hat{\boldsymbol{u}} \cdot \boldsymbol{n}, 1 \rangle_{\partial \Omega^e} = 0 \quad \text{for } e = 1, \ldots, m_{el}, \\
&\hat{\boldsymbol{u}} = \mathbb{P}_2(\bar{\boldsymbol{u}}) \quad \text{on } \partial \Omega_D,
\end{aligned}
\tag{29a}
$$

$$
\begin{aligned}
&\sum_{e=1}^{m_{el}} \langle \delta \hat{\theta}, (\boldsymbol{q} + \hat{\boldsymbol{u}} \hat{\theta}) \cdot \boldsymbol{n} + \tau_\theta (\theta - \hat{\theta}) \rangle_{\partial \Omega^e} = \langle \delta \hat{\theta}, \bar{q}_n \rangle_{\partial \Omega_N}, \\
&\hat{\theta} = \mathbb{P}_2(\bar{\theta}) \quad \text{on } \partial \Omega_D,
\end{aligned}
\tag{29b}
$$

for all $(\delta \boldsymbol{u}, \delta p, \delta \boldsymbol{L}, \delta \theta, \delta \boldsymbol{q}, \delta \hat{\boldsymbol{u}}, \delta \hat{\theta}) \in [\mathcal{V}^h]^d \times \mathcal{V}^h \times [\mathcal{V}^h]^{d \times d} \times \mathcal{V}^h \times [\mathcal{V}^h]^d \times [\Lambda^h]^d \times \Lambda^h$ such that $\delta \hat{\boldsymbol{u}} = \boldsymbol{0}$ and $\delta \hat{\theta} = 0$ on $\partial \Omega_D$, where the discrete spaces are defined in (12) taking $\Omega = \Omega_D$. $\mathbb{P}_2(\bar{\boldsymbol{u}})$ and $\mathbb{P}_2(\bar{\theta})$ are the $\mathcal{L}_2$ projections of the Dirichlet data into the approximation space on $\partial \Omega_D$. The parameters τ_u and τ_θ are positive and, following [36,33], they are usually taken as

$$
\tau_u \approx \frac{\nu}{L} + |\boldsymbol{u}|, \qquad \tau_\theta \approx \frac{\alpha}{L} + |\boldsymbol{u} \cdot \boldsymbol{n}|, \tag{30}
$$

where L is the characteristic length of the problem. Even though the so-called stabilization parameter has some influence on the accuracy of the HDG solution, the method is very robust in front of variations of τ_u and τ_θ [33,34]. Nevertheless, as will be seen in the numerical tests in section 4.4, choosing this parameter according to equation (30) is crucial to alleviate or remove numerical oscillations in the presence of sharp fronts.

The discretization of local and global problems (28)-(29) leads to a discrete residual of the form,

$$\left[\begin{array}{ccc:ccccccc}
\mathbf{A}_{\hat{u}\hat{u}} & \mathbf{0} & \mathbf{0} & \mathbf{A}_{\hat{u}u} & \mathbf{A}_{\hat{u}L} & \mathbf{A}_{\hat{u}p} & \mathbf{0} & \mathbf{0} & \mathbf{0} \\
\mathbf{A}_{\rho\hat{u}} & \mathbf{0} & \mathbf{0} & \mathbf{0} & \mathbf{0} & \mathbf{0} & \mathbf{0} & \mathbf{0} & \mathbf{0} \\
\mathbf{0} & \mathbf{0} & \mathbf{A}_{\hat{\theta}\hat{\theta}} + \mathbf{C}_{\hat{\theta}\hat{\theta}}(\hat{\mathbf{u}}) & \mathbf{0} & \mathbf{0} & \mathbf{0} & \mathbf{0} & \mathbf{A}_{\hat{\theta}\theta} & \mathbf{A}_{\hat{\theta}q} \\
\hdashline
\mathbf{A}_{u\hat{u}} + \mathbf{C}_{u\hat{u}}(\hat{\mathbf{u}}) & \mathbf{0} & \mathbf{0} & \mathbf{A}_{uu} + \mathbf{C}_{uu}(\mathbf{u}) & \mathbf{A}_{uL} & \mathbf{A}_{up} & \mathbf{0} & \mathbf{A}_{u\theta} & \mathbf{0} \\
\mathbf{A}_{L\hat{u}} & \mathbf{0} & \mathbf{0} & \mathbf{A}_{Lu} & \mathbf{A}_{LL} & \mathbf{0} & \mathbf{0} & \mathbf{0} & \mathbf{0} \\
\mathbf{A}_{p\hat{u}} & \mathbf{0} & \mathbf{0} & \mathbf{A}_{pu} & \mathbf{0} & \mathbf{0} & \mathbf{A}_{\rho p}^{T} & \mathbf{0} & \mathbf{0} \\
\mathbf{0} & -\mathbf{1} & \mathbf{0} & \mathbf{0} & \mathbf{0} & \mathbf{A}_{\rho p} & \mathbf{0} & \mathbf{0} & \mathbf{0} \\
\mathbf{0} & \mathbf{0} & \mathbf{A}_{\theta\hat{\theta}} + \mathbf{C}_{\theta\hat{\theta}}(\hat{\mathbf{u}}) & \mathbf{0} & \mathbf{0} & \mathbf{0} & \mathbf{0} & \mathbf{A}_{\theta\theta} + \mathbf{C}_{\theta\theta}(\mathbf{u}) & \mathbf{A}_{\theta q} \\
\mathbf{0} & \mathbf{0} & \mathbf{A}_{q\hat{\theta}} & \mathbf{0} & \mathbf{0} & \mathbf{0} & \mathbf{0} & \mathbf{A}_{q\theta} & \mathbf{A}_{qq}
\end{array}\right]
\left\{\begin{array}{c}
\hat{\mathbf{u}} \\ \boldsymbol{\rho} \\ \hat{\boldsymbol{\theta}} \\ \hdashline \mathbf{u} \\ \mathbf{L} \\ \mathbf{p} \\ \boldsymbol{\lambda} \\ \boldsymbol{\theta} \\ \mathbf{q}
\end{array}\right\}
-
\left\{\begin{array}{c}
\bar{\mathbf{t}} \\ \mathbf{0} \\ \bar{\mathbf{q}}_n \\ \hdashline \bar{\mathbf{f}}_{\theta_0} + \bar{\mathbf{s}} \\ \mathbf{0} \\ \mathbf{0} \\ \mathbf{0} \\ \bar{\mathbf{g}} \\ \mathbf{0}
\end{array}\right\} = \mathbf{0}. \tag{31}$$

This coupled system is solved in a monolithic sense using Newton–Raphson method computing the exact Jacobian matrix. As already explained in previous sections, static condensation is used to express the local variables in terms of global variables and solve the final system in only global unknowns. The constraint in (28b) is applied using a Lagrangian multiplier λ_e on each element. These are gathered in the vector $\boldsymbol{\lambda}$. The matrices in the system (31) that arise from Navier–Stokes are presented in the appendix of an earlier work [38], while the matrices from convection-diffusion and the matrices that result from the coupling are presented in the appendix, along with their tangent operators.

The HDG formulation provides a numerical solution with optimal convergence of order $k+1$ (k is the degree of approximation) in $\mathcal{L}_2$ norm for velocity, $\boldsymbol{u}$, pressure, p, gradient of velocity, $\boldsymbol{L}$, temperature, θ, and flux, $\boldsymbol{q}$. As the mean of the velocity and mean of the temperature inside each element converges with order $k+2$, new approximate solutions for $\boldsymbol{u}$ and θ can be computed element-by-element which converge with order $k+2$. The details of the post-processing are explained in the literature for Navier–Stokes [36] and convection-diffusion [33] equations. In the present work, it is concluded that the property of super-convergence is retained in the case of the Navier–Stokes/convection-diffusion coupled formulation for both velocity and temperature, as will be shown in the numerical example in the next section.

4.3 Convergence results

In this section, the convergence results of Navier–Stokes equations coupled with convection-diffusion equation are presented for HDG. The solution of Navier–Stokes equations is taken as Kovasznay flow [28], which is the analytical solution of Navier–Stokes in domain $[0,2]\times[-0.5,1.5]$. The analytical solution considered for the temperature variation is of sinusoidal form. The expressions

for velocity, pressure and temperature are given as follows,

$$\begin{aligned} \boldsymbol{u} &= \begin{bmatrix} 1 - \exp(\lambda x_1)\cos(2\pi x_2) \\ \dfrac{\lambda}{2\pi}\exp(\lambda x_1)\cos(2\pi x_2) \end{bmatrix}, \\ p &= -\frac{1}{2}\exp(2\lambda x_1) + C, \\ \theta &= \sin\left(\frac{3\pi x_1}{4}\right)\sin\left(\frac{3\pi x_2}{4} + \frac{3\pi}{8}\right), \end{aligned} \tag{32}$$

where $\lambda = \frac{Re}{2} - \sqrt{\frac{Re^2}{4} + 4\pi^2}$ and $Re = \frac{1}{\nu}$ is the Reynolds number. Dirichlet boundary conditions are prescribed for velocity and temperature on all the exterior boundary. The solution is computed at $Re = 20$ and the thermal diffusivity, α, is taken as unity.

As discussed earlier, the Boussinesq approximation term couples the Navier–Stokes and convection-diffusion equations. In the Boussinesq term (26), β is taken as unity, $\boldsymbol{g} = -10\boldsymbol{e}_2$ and $\theta_0 = 0$. An appropriate body force term, $\bar{\boldsymbol{s}}$ in momentum equation, and heat generation, $\bar{g}$, in the convection-diffusion equation are computed from the analytical solution. The body force term, $\bar{\boldsymbol{s}}$, is considered only in the convergence analysis, while this term is taken as zero in Rayleigh–Bénard convection flow and conjugate heat transfer problems. The parameters, τ_u and τ_θ, are both taken as unity on all faces of each element in this example.

Figure 8 shows the convergence of post-processed solution of velocity and temperature for triangular meshes for degree $k = 2 - 9$ and element size, $h = 2/\{2, 4, 8, 16, 32, 64\}$. It is clear that the super-convergence of HDG is retained for both velocity and temperature in the coupled framework.

As the extension of our previous work [38], the results of computational efficiency of HDG (P_k) and CG (P_kP_{k-1}) are presented for the coupled Navier–Stokes/convection-diffusion equations. Taylor–Hood [45] elements are used for CG discretization of Navier–Stokes equations with velocities approximated with polynomial of degree k and pressure with $k-1$. Here, only the plots of the ratio of CPU times of HDG to CG against the error are presented. Note that CPU times of solving only the final linear system is taken into account in the plots. The time taken to compute the elemental matrices and assemble them is highly implementation dependent and they can be parallelized relatively easily. In the present implementation, direct solvers are used as black boxes as mentioned previously in Section 3.4. Hence, only CPU times of the global solve are taken into account to have a robust comparison in terms of computational efficiency. Figures 9 and 10 show the ratio of CPU times with respect to error in velocity and ratio of CPU times with respect to error in temperature, respectively. As explained in the mentioned work, the errors values from CG are used in plots and CPU times of HDG are interpolated corresponding to the errors of CG. Note that post-processed solutions are used to compute errors in HDG for both velocity and temperature. From the results, it can be concluded that HDG outperforms CG in terms of CPU time for linear solver for a given level accuracy and $k \geq 3$. Hence, the conclusions drawn from the

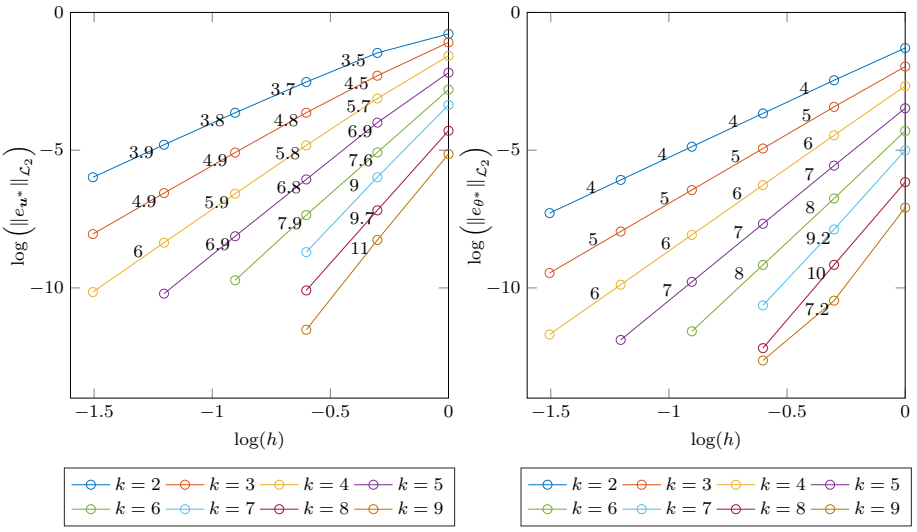

(a) $\boldsymbol{u}^*$. (b) θ^*.

Fig. 8: Coupled Navier–Stokes/convection-diffusion problem: convergence plots for post-processed velocity and post-processed temperature with HDG(P_k) using triangular elements.

computational efficiency for Navier–Stokes can be extended to the present coupled Navier–Stokes/convection-diffusion analysis.

4.4 Rayleigh–Bénard convection flow

This section presents the results of Rayleigh–Bénard convection flow at different Rayleigh numbers. This is a standard benchmark example for natural buoyancy flows.

A square cavity of unit length is considered with a temperature gradient along x_1-direction. The top and bottom walls are prescribed with adiabatic boundary conditions, whereas the laterals walls are prescribed with Dirichlet boundary conditions for temperature. No-slip conditions are applied on all the boundary for the velocity. Rayleigh numbers ranging from 10^3 to 10^8, along with Prandtl number of 0.71, are considered in the analysis. The temperature difference is kept at unity with left wall at 0.5 and right wall at -0.5, $\boldsymbol{g} = -10\boldsymbol{e}_2$ and β is chosen based on the Ra. Nusselt number at the hot wall is used to compare the HDG (P_k) solution with CG (P_kP_{k-1}) and other results from literature. Average Nusselt number is defined as,

$$Nu = -\frac{1}{\theta_h - \theta_c}\int_0^L \frac{\partial\theta}{\partial x_1}\mathrm{d}s, \tag{33}$$

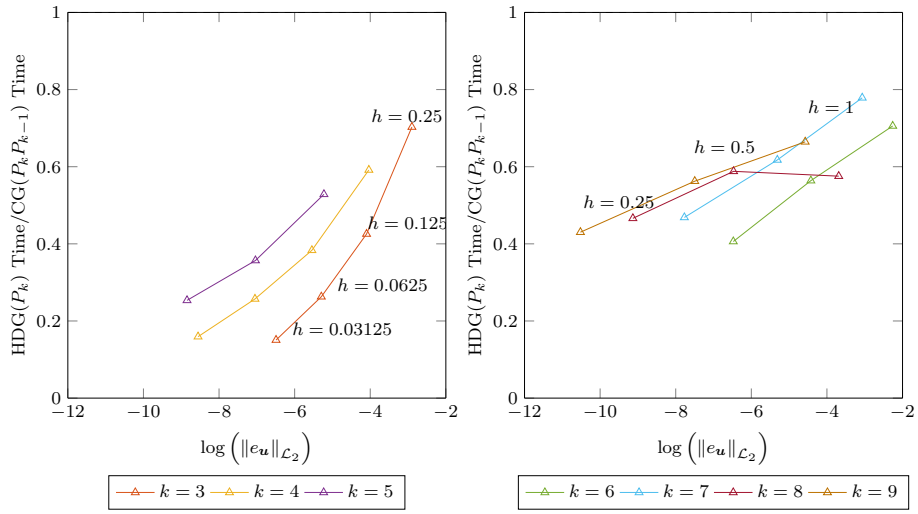

(a) $k = 3 - 5$. (b) $k = 6 - 9$.

Fig. 9: Coupled Navier–Stokes/convection-diffusion problem: ratio of CPU times for linear solver *vs.* error in velocity for triangular elements.

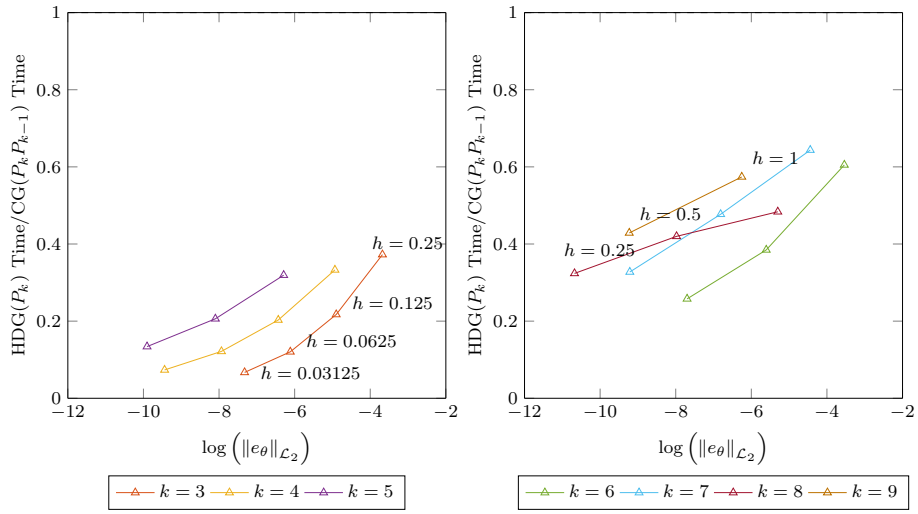

(a) $k = 3 - 5$. (b) $k = 6 - 9$.

Fig. 10: Coupled Navier–Stokes/convection-diffusion problem: ratio of CPU times for linear solver *vs.* error in temperature for triangular elements.

Table 1: Rayleigh–Bénard convection flow: τ_u, τ_θ parameters

Ra	τ_u, τ_θ
10^3, 10^4	1
10^5	10
10^6	100
10^7, 10^8	500

where θ_h and θ_c denote the temperatures of hot and cold walls and L is the length of the cavity.

A uniform mesh with triangular elements of degree $k = 5$ and element size $h = 1/2^6$ was chosen. All the results presented corresponds to steady state analysis. Sometimes, at higher Rayleigh number, convergence to the solution could not be achieved in a single step. In this case, Ra number is increased in a finite number of steps to obtain a converged solution. No stabilization techniques for the CG method are used.

The parameters, τ_u, τ_θ, in the case of HDG discretization are critical in obtaining a solution at higher Ra. Table 1 provides the values of parameters used in the present work for different Ra. The analytical maximum velocity in the domain increases with increasing Ra number. In the present work, the parameters, τ_u, τ_θ, are chosen to be in the order of magnitude of the maximum velocity in the domain for a given Ra.

Figure 11 presents the isolines of velocity and temperature at Ra of $10^4, 10^6$ and 10^8. It can be noticed from the plots that as the Ra number increases, a strong boundary layer is formed at both lateral edges of the domain. The vertical isotherms denote that the dominant mechanism of heat transfer is conduction and as the isoterms depart from the vertical position, convection becomes the dominant form of heat transfer. It is evident from the velocity isolines that velocity varies from 20 at $Ra = 10^4$ to around 2200 at $Ra = 10^8$.

The variation of dimensionless u_1 along $x_1 = 0.5$ and dimensionless u_2 along $x_2 = 0.5$ are presented in figs. 12a and 12b, respectively, to show the evolution of boundary layer as the Ra increases. Similarly, the variation of temperature along $x_2 = 0.5$ is plotted for all the Ra numbers considered in fig. 12c. The present numerical results are compared with [6] whenever applicable and the values are denoted by circle marks in the plots. The fact that HDG could resolve the boundary layer without any refinement on boundary shows the effectiveness of using high-order meshes.

To validate the results obtained in the present work, various quantities of interest are compared with the results from literature. The comparison is presented in the tables 2 and 3, which shows the results of HDG, CG and the literature ones. The table presents the results of both HDG and CG with that of literature ones. The results from HDG and CG are practically similar owing to the high-degree of the approximations and relatively refined mesh. Nevertheless, HDG produces slightly more accurate solution than CG when Nusselt number is compared for $Ra = 10^8$. However, when CPU times for the linear solver are considered, HDG outperforms CG in the present example

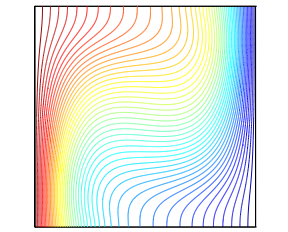

(a) Temperature, $Ra = 10^4$.

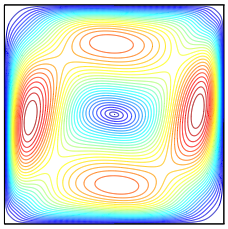

(b) Velocity, $Ra = 10^4$.

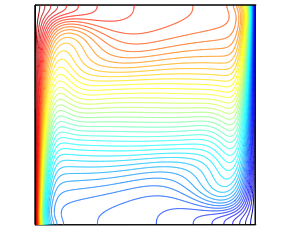

(c) Temperature, $Ra = 10^6$.

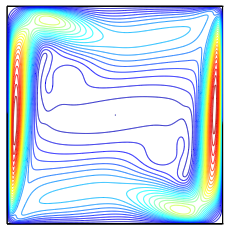

(d) Velocity, $Ra = 10^6$.

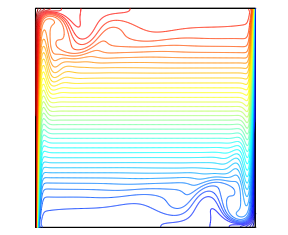

(e) Temperature, $Ra = 10^8$.

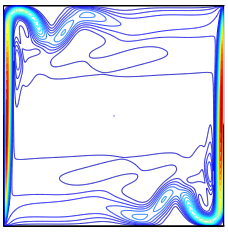

(f) Velocity, $Ra = 10^8$.

Fig. 11: Rayleigh–Bénard convection flow: isolines of temperature and velocity at different Ra numbers using HDG.

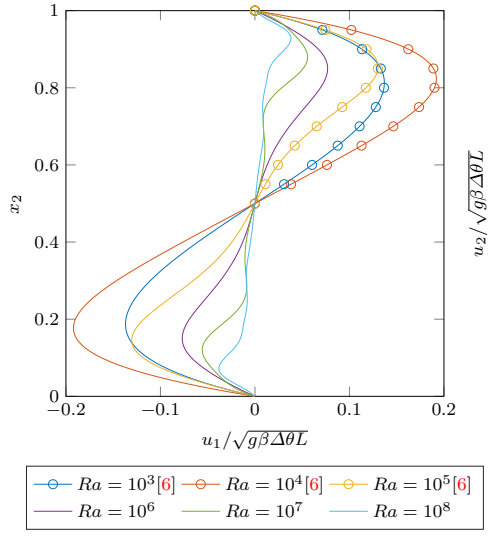

(a) Dimensionless u_1.

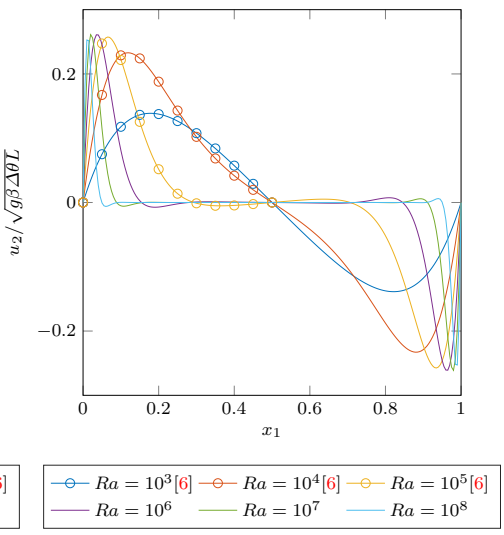

(b) Dimensionless u_2.

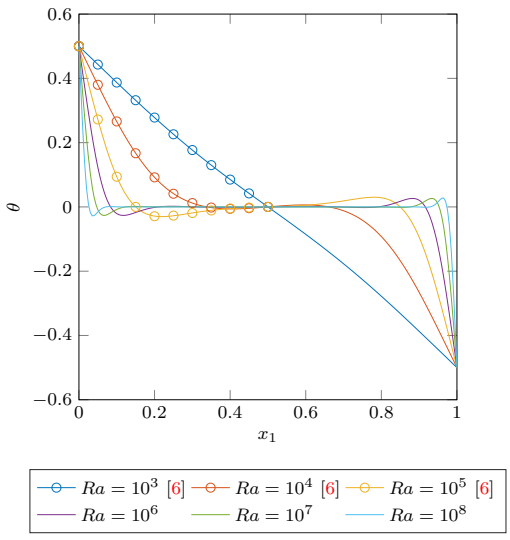

(c) Temperature, θ.

Fig. 12: Rayleigh–Bénard convection flow: distribution of temperature and velocity components at different Ra numbers using HDG. Circles correspond to reference values in [6].

Table 2: Rayleigh–Bénard convection flow: summary of important quantities and comparison with literature values for $Ra = 10^3 - 10^5$.

Ra	Quantity	De Vahl Davis [18]	HDG (P_5) / CG (P_5P_4)
10^3	Nu	1.117	1.117
	Max. u_1 along $x_1 = 0.5$	3.649	3.649
	Max. u_2 along $x_2 = 0.5$	3.697	3.697
10^4	Nu	2.238	2.244
	Max. u_1 along $x_1 = 0.5$	16.178	16.183
	Max. u_2 along $x_2 = 0.5$	19.617	16.626
10^5	Nu	4.509	4.521
	Max. u_1 along $x_1 = 0.5$	34.73	34.740
	Max. u_2 along $x_2 = 0.5$	68.59	68.632

Table 3: Rayleigh–Bénard convection flow: summary of important quantities and comparison with literature values for $Ra = 10^6 - 10^8$.

Ra	Quantity	Le Quéré [30]	HDG (P_5)	CG (P_5P_4)
10^6	Nu	8.825	8.825	8.825
	Max. u_1 along $x_1 = 0.5$	64.83	64.826	64.826
	Max. u_2 along $x_2 = 0.5$	220.6	220.390	220.390
10^7	Nu	16.523	16.523	16.521
	Max. u_1 along $x_1 = 0.5$	148.580	148.583	148.583
	Max. u_2 along $x_2 = 0.5$	699.236	695.940	695.940
10^8	Nu	30.225	30.209	30.145
	Max. u_1 along $x_1 = 0.5$	321.876	321.567	321.568
	Max. u_2 along $x_2 = 0.5$	2222.39	2221.647	2221.657

Table 4: Rayleigh–Bénard convection flow: computational details for HDG and CG for $Ra = 10^5$ and $h = 1/2^6$.

	HDG (P_5)	CG (P_5P_4)
DOFs	231680	203140
CPU time for linear solver	67.8 sec	75 sec
No. of non-linear iterations	13	13
Condition number, $\kappa(\mathbf{A})$	$\mathcal{O}(10^{11})$	$\mathcal{O}(10^{12})$
No. of non-zeros, nnz	20,478,391	19,854,033

using a uniform triangular mesh with $h = 1/2^6$ and $k = 5$. Table 4 gives the details of computations for HDG and CG at $Ra = 10^5$. Even though, HDG has slightly more DOFs than CG, the CPU time for the linear solver per one non-linear iteration of HDG is less than its CG counterpart. This can be attributed towards the regular block structure of the HDG stiffness matrix in accordance with the study in [27,48]. This fact is more pronounced by comparing the condition numbers of the matrix, which is one order of magnitude larger for CG than for HDG, for same mesh and degree of approximation.

Hence, it can be advantageous to use high-order HDG methods to solve the coupled Navier–Stokes/convection-diffusion equations, specially in the presence of strong boundary layers.

5 Coupled CG-HDG formulation for conjugate heat transfer problem

Following fig. 13, consider Ω_D is the fluid domain and Ω_C is the solid part. The governing equations for Ω_D are presented in (24), while the solid domain Ω_C is governed by heat equation presented in (4c). Since, the interface boundary is solid wall, no-slip boundary condition is applied for fluid, *i.e.*, velocity is zero on the interface. Therefore, convective flux entering the solid domain is zero and the transmission conditions presented in (4f) and (4g) are valid in this example. The extension of coupled formulation presented in section 3 to the conjugate heat transfer problem is straightforward.

Here the coupling is made between heat equation in Ω_C and the diffusive flux term of the convection-diffusion equation in Ω_D. Hence, the system of equations in (13) can be readily expressed along with coupled Navier–Stokes/convection-diffusion equations in (31) to obtain the residual in the matrix notation in (34).

$$
\left[\begin{array}{cccc:cccccc}
\mathbf{A}_{\hat{u}\hat{u}} & \mathbf{0} & \mathbf{0} & \mathbf{0} & \mathbf{A}_{\hat{u}u} & \mathbf{A}_{\hat{u}L} & \mathbf{A}_{\hat{u}p} & \mathbf{0} & \mathbf{0} & \mathbf{0} \\
\mathbf{A}_{\rho\hat{u}} & \mathbf{0} & \mathbf{0} & \mathbf{0} & \mathbf{0} & \mathbf{0} & \mathbf{0} & \mathbf{0} & \mathbf{0} & \mathbf{0} \\
\mathbf{0} & \mathbf{0} & \mathbf{A}_{\hat{\theta}\hat{\theta}} + \mathbf{C}_{\hat{\theta}\hat{\theta}}(\hat{\mathbf{u}}) & \mathbf{0} & \mathbf{0} & \mathbf{0} & \mathbf{0} & \mathbf{0} & \mathbf{A}_{\hat{\theta}\theta} & \mathbf{A}_{\hat{\theta}q} \\
\mathbf{0} & \mathbf{0} & \mathbf{0} & \mathbf{K}_{\theta\theta} & \mathbf{0} & \mathbf{0} & \mathbf{0} & \mathbf{0} & \mathbf{B}_{\theta\theta}^T & \mathbf{B}_{\theta q} \\
\hdashline
\mathbf{A}_{u\hat{u}} + \mathbf{C}_{u\hat{u}}(\hat{\mathbf{u}}) & \mathbf{0} & \mathbf{0} & \mathbf{0} & \mathbf{A}_{uu} + \mathbf{C}_{uu}(\mathbf{u}) & \mathbf{A}_{uL} & \mathbf{A}_{up} & \mathbf{0} & \mathbf{A}_{u\theta} & \mathbf{0} \\
\mathbf{A}_{L\hat{u}} & \mathbf{0} & \mathbf{0} & \mathbf{0} & \mathbf{A}_{Lu} & \mathbf{A}_{LL} & \mathbf{0} & \mathbf{0} & \mathbf{0} & \mathbf{0} \\
\mathbf{A}_{p\hat{u}} & \mathbf{0} & \mathbf{0} & \mathbf{0} & \mathbf{A}_{pu} & \mathbf{0} & \mathbf{0} & \mathbf{A}_{\rho p}^T & \mathbf{0} & \mathbf{0} \\
\mathbf{0} & -\mathbf{1} & \mathbf{0} & \mathbf{0} & \mathbf{0} & \mathbf{0} & \mathbf{A}_{\rho p} & \mathbf{0} & \mathbf{0} & \mathbf{0} \\
\mathbf{0} & \mathbf{0} & \mathbf{A}_{\theta\hat{\theta}} + \mathbf{C}_{\theta\hat{\theta}}(\hat{\mathbf{u}}) & \mathbf{B}_{\theta\theta} & \mathbf{0} & \mathbf{0} & \mathbf{0} & \mathbf{0} & \mathbf{A}_{\theta\theta} + \mathbf{C}_{\theta\theta}(\mathbf{u}) & \mathbf{A}_{\theta q} \\
\mathbf{0} & \mathbf{0} & \mathbf{A}_{q\hat{\theta}} & \mathbf{B}_{q\theta} & \mathbf{0} & \mathbf{0} & \mathbf{0} & \mathbf{0} & \mathbf{A}_{q\theta} & \mathbf{A}_{qq}
\end{array}\right]
\left\{\begin{array}{c}
\hat{\mathbf{u}} \\ \boldsymbol{\rho} \\ \hat{\boldsymbol{\theta}}_D \\ \boldsymbol{\theta}_C \\ \hdashline \mathbf{u} \\ \mathbf{L} \\ \mathbf{p} \\ \boldsymbol{\lambda} \\ \boldsymbol{\theta}_D \\ \mathbf{q}_D
\end{array}\right\}
-
\left\{\begin{array}{c}
\bar{\mathbf{t}} \\ \mathbf{0} \\ \bar{\mathbf{q}}_n \\ \bar{\mathbf{g}}_C \\ \hdashline \bar{\mathbf{f}}_{\theta_0} \\ \mathbf{0} \\ \mathbf{0} \\ \mathbf{0} \\ \bar{\mathbf{g}}_D \\ \mathbf{0}
\end{array}\right\}
= \mathbf{0}. \tag{34}
$$

The matrix $\mathbf{A}_{u\theta}$ couples temperature to the momentum equation and the matrices $\mathbf{C}_{\theta\hat{\theta}}(\hat{\mathbf{u}})$, $\mathbf{C}_{\theta\theta}(\mathbf{u})$ couples velocity from Navier–Stokes to convection-diffusion equation. Following the static condensation technique, only unknowns in $\hat{\mathbf{u}}, \boldsymbol{\rho}, \hat{\boldsymbol{\theta}}_D$ and $\boldsymbol{\theta}_C$ are solved in the final system and local variables are computed element-by-element.

5.1 Conjugate heat transfer problem

In this example, the proposed models are combined together to solve a benchmark conjugate heat transfer problem. The fluid part, which is governed by Navier–Stokes/convection-diffusion, is discretized using HDG, while the solid part, governed by heat equation, is discretized using CG.

The geometry of the problem along with the applied boundary conditions are shown in fig. 13. The fluid domain, Ω_D, is the square cavity of unit length and the solid wall, Ω_C, has a thickness of 0.2. The ratio of thermal diffusivities of solid to fluid is considered as unity. Prandtl number of 0.71 is used in Ω_D in the computations.

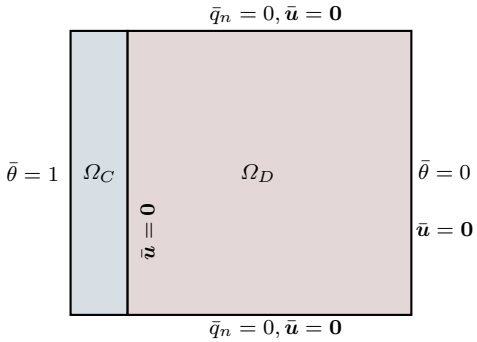

Fig. 13: Conjugate heat transfer problem: geometry and prescribed boundary values of conjugate heat transfer problem domain.

The problem is solved with the proposed CG(Q_{k+1})-HDG(Q_k) model and, also, a CG(Q_{k+1})-CG($Q_{k+1}Q_k$) model, where all the equations are discretized with CG method. The solution is approximated with one degree higher in the CG domain than HDG, to keep the optimal convergence in both domains, as discussed in section 3. The obtained results are compared with the literature data. A degree of approximation $k = 5$, and an uniform mesh size, $h = 0.025$, with quadrilateral elements are used in both models. As stated in the section 4.4, at higher Ra number, an incremental method is used to obtain the steady state numerical solution. The parameters, τ_u, τ_θ, are the same as in table 1.

Figure 14 presents the isolines for velocity and temperature at different Ra number. The temperature and velocity distributions inside the fluid cavity are similar to the solutions of Rayleigh–Bénard convection flow with relatively less sharp boundary layer. At higher Ra, the loss of symmetry in the solution of velocity can be clearly noticed in the present example.

Nusselt number at the fluid-solid interface is computed and compared with the values present in the literature. Whenever possible, the average temperature on the interface is also compared with literature data. It is to be noted that the geometry considered in the work of [26] has the solid wall to the right of fluid domain. Hence, the results presented for the comparison with the mentioned work correspond to the solid wall to the right of fluid domain. All the results obtained by both models are presented in table 5 and, for the number of significant digits presented, they coincide. They are also very close to the literature values.

The models will be now compared in terms of computational effort to point their relative merits. The computational details of CG(Q_{k+1})-HDG(Q_k) and CG(Q_{k+1})-CG($Q_{k+1}Q_k$) models are tabulated in table 6, similar to one presented for Rayleigh–Bénard convection flow. It is clear from this table that the proposed CG-HDG model is superior to CG-CG model in terms of computational efficiency and complexity. It is also worth stressing that both models have similar orders of convergence for all the variables of interest. Hence, the

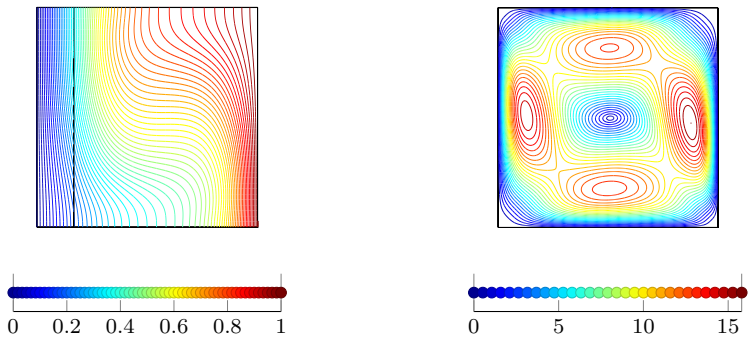

(a) Temperature, $Ra = 10^4$. (b) Velocity, $Ra = 10^4$.

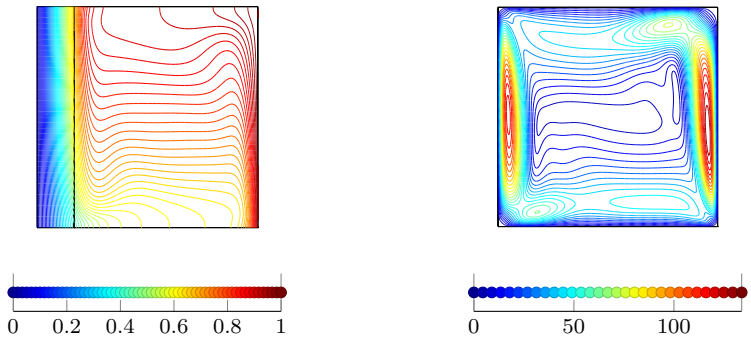

(c) Temperature, $Ra = 10^6$. (d) Velocity, $Ra = 10^6$.

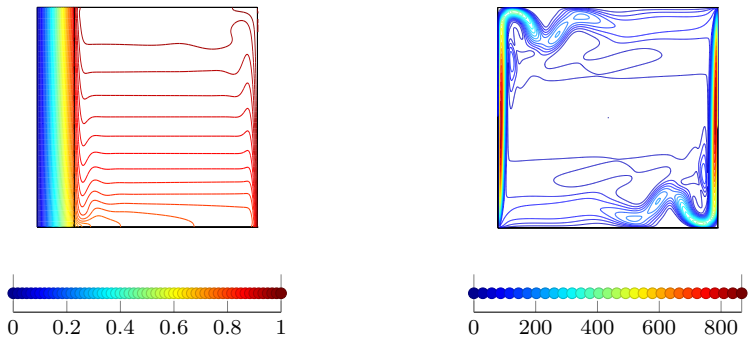

(e) Temperature, $Ra = 10^8$. (f) Velocity, $Ra = 10^8$.

Fig. 14: Conjugate heat transfer problem: isolines of temperature and velocity at different Ra numbers using CG-HDG model.

Table 5: Conjugate heat transfer problem: summary of important quantities and comparison with literature values for $Ra = 10^3 - 10^8$.

Ra	Quantity	Misra & Sarkar [32]	Kaminski & Prakash [26]	CG(Q_6)-HDG(Q_5) / CG(Q_6)-CG(Q_6Q_5)
0.7×10^3	Nu	—	0.87	0.8678
	Mean θ along interface	—	—	0.8264
10^3	Nu	0.8958	—	0.8957
	Mean θ along interface	0.1791	—	0.1791
10^4	Nu	1.4528	—	1.4537
	Mean θ along interface	0.2906	—	0.2906
0.7×10^5	Nu	—	2.08	2.0850
	Mean θ along interface	—	—	0.5832
10^5	Nu	2.1997	—	2.2014
	Mean θ along interface	0.4400	—	0.4400
0.7×10^6	Nu	—	2.87	2.8540
	Mean θ along interface	—	—	0.4294
10^6	Nu	2.9528	—	2.9605
	Mean θ along interface	0.5916	—	0.5919
0.7×10^7	Nu	—	3.53	3.5077
	Mean θ along interface	—	—	0.2987
10^7	Nu	—	—	3.5913
	Mean θ along interface	—	—	0.7181
10^8	Nu	—	—	4.061
	Mean θ along interface	—	—	0.8120

Table 6: Conjugate heat transfer problem: computational details for CG-HDG and CG-CG for $Ra = 10^5$ and $h = 0.025$.

	CG(Q_6)-HDG(Q_5)	CG(Q_6)-CG(Q_6Q_5)
DOFs	64209	72612
CPU time for linear solver	13.3 sec	25.5 sec
No. of non-linear iterations	11	11
Condition number, $\kappa(\mathbf{A})$	$\mathcal{O}(10^{10})$	$\mathcal{O}(10^{12})$
No. of non-zeros, nnz	7,377,875	11,033,375

proposed CG-HDG model can be beneficial to use for multi-physics flows involving high Ra number.

6 Conclusions

Optimal HDG and CG convergence rates are kept with both CG-HDG coupled formulations proposed for the heat equation when the degree of approximation for CG is one degree higher than HDG degree.

Optimal convergence and super-convergence rates are shown in the numerical tests for the coupled Navier–Stokes/convection-diffusion equations formulation with HDG. The results of Rayleigh–Bénard convection flow are presented until Ra of 10^8 and the Nusselt numbers are compared between HDG, CG and literature values. Even though, both HDG and CG can resolve the solution at high Ra, it is noticed that HDG is more accurate and has less computational

cost. CPU times for linear solver and condition numbers of HDG are lower than its CG counterpart for the same mesh and degree of approximation in the example considered.

Finally, the proposed CG-HDG coupling is merged with coupled HDG formulation for Navier–Stokes/convection-diffusion equations and applied to a conjugate heat transfer problem. The benchmark problem is solved using both CG-HDG and CG-CG models and the results are compared to literature data. Both models give the identical results in terms of Nusselt numbers and mean temperature on interface, but, it is shown that CG-HDG model has higher computational efficiency than CG-CG model.

Acknowledgements This work was supported by the Erasmus Mundus Joint Doctorate SEED project (European Commission, 2013-1436/001-001-EMJD). The work of the second author is part of the research activity carried out at Civil Engineering Research and Innovation for Sustainability (CERIS) and has been partially financed by Fundação para a Ciência e a Tecnologia (FCT) in the framework of project UID/ECI/04625/2013. The third author also wishes to acknowledge the DAFOH2 project (Ministerio de Economia y Competitividad, MTM2013-46313-R) and the Catalan government (Generalitat de Catalunya, 2009SGR875).

Appendix: Definition of elemental matrices

In this appendix, the elemental matrices that arise from coupled CG-HDG formulation for heat equation and HDG method for coupled Navier–Stokes/convection-diffusion equations are defined. All the variables presented in this section are the elemental variables. Variable $\boldsymbol{L}^{(e)}$ is a second–order tensor and it is represented as a column vector, $[l_{11}\, l_{12}\, l_{21}\, l_{22}]^{(e)T}$, in the numerical computations.

The independent variables $(\boldsymbol{L}^{(e)}, \boldsymbol{u}^{(e)}, p^{(e)}, \theta^{(e)}, \boldsymbol{q}^{(e)}, \hat{\boldsymbol{u}}^{(e)}, \rho^{(e)}, \hat{\theta}^{(e)})$ over each element, Ω^e, can be approximated as follows,

$$\begin{aligned}
\boldsymbol{L}^{(e)}(\boldsymbol{\xi}) = \boldsymbol{\psi}_L(\boldsymbol{\xi})\mathbf{L}^{(e)}, \quad \boldsymbol{u}^{(e)}(\boldsymbol{\xi}) = \boldsymbol{\psi}_u(\boldsymbol{\xi})\mathbf{u}^{(e)}, \quad p^{(e)}(\boldsymbol{\xi}) = \boldsymbol{\psi}_p(\boldsymbol{\xi})\mathbf{p}^{(e)} \quad &\text{in} \quad \Omega^e,\\
\theta^{(e)}(\boldsymbol{\xi}) = \boldsymbol{\psi}_\theta(\boldsymbol{\xi})\boldsymbol{\theta}^{(e)}, \quad \boldsymbol{q}^{(e)}(\boldsymbol{\xi}) = \boldsymbol{\psi}_q(\boldsymbol{\xi})\mathbf{q}^{(e)} \quad &\text{in} \quad \Omega^e,\\
\hat{\boldsymbol{u}}^{(e)}(\xi) = \boldsymbol{\psi}_{\hat{u}}(\xi)\hat{\mathbf{u}}^{(e)}, \quad \hat{\theta}^{(e)}(\xi) = \boldsymbol{\psi}_{\hat{\theta}}(\xi)\hat{\boldsymbol{\theta}}^{(e)} \quad &\text{on} \quad \partial\Omega^e,
\end{aligned} \tag{35}$$

where $\boldsymbol{\psi}_L(\boldsymbol{\xi})$, $\boldsymbol{\psi}_u(\boldsymbol{\xi})$, $\boldsymbol{\psi}_p(\boldsymbol{\xi}), \boldsymbol{\psi}_\theta(\boldsymbol{\xi}), \boldsymbol{\psi}_q(\boldsymbol{\xi}), \boldsymbol{\psi}_{\hat{u}}(\xi)$ and $\boldsymbol{\psi}_{\hat{\theta}}(\xi)$ are matrices that gather the approximation functions of respective unknowns, while $\mathbf{L}^{(e)}$, $\mathbf{u}^{(e)}$, $\mathbf{p}^{(e)}, \boldsymbol{\theta}^{(e)}, \mathbf{q}^{(e)}, \hat{\mathbf{u}}^{(e)}$ and $\hat{\boldsymbol{\theta}}^{(e)}$ are the elemental nodal column vectors of gradient of velocity, velocity, pressure, temperature, flux, velocity trace and temperature trace, respectively. $\boldsymbol{\xi}$ and ξ represent the coordinate in the area and line reference domains, respectively. $\hat{\mathbf{u}}^{(e)}$ contains the trace of velocity on each face of the element and it can be represented as $\left[\hat{\mathbf{u}}^{\mathbf{F}_{e1}} \ldots \hat{\mathbf{u}}^{\mathbf{F}_{en}}\right]^T$, where $\mathbf{F}_{ef}$ is the f^{th} face of e^{th} element. Here, $n = 3$ in the case of triangular elements, while $n = 4$ for quadrilateral elements. From now on explicit dependence on $\boldsymbol{\xi}$ and

ξ will be omitted for the sake of simplicity. The approximation functions can be represented as follows,

$$\begin{aligned}
\boldsymbol{\psi}_L &= \begin{bmatrix} \boldsymbol{\psi} & & & \\ & \boldsymbol{\psi} & & \\ & & \boldsymbol{\psi} & \\ & & & \boldsymbol{\psi} \end{bmatrix}, \quad \boldsymbol{\psi}_u = \boldsymbol{\psi}_q = \begin{bmatrix} \boldsymbol{\psi} & \\ & \boldsymbol{\psi} \end{bmatrix}, \quad \boldsymbol{\psi}_p = \boldsymbol{\psi}_\theta = \boldsymbol{\psi}, \\
\boldsymbol{\psi}_{\hat{u}} &= \begin{bmatrix} \boldsymbol{\psi}_{\mathbf{F}_{e1}} & & \cdots & \boldsymbol{\psi}_{\mathbf{F}_{en}} \\ & \boldsymbol{\psi}_{\mathbf{F}_{e1}} \cdots & & \boldsymbol{\psi}_{\mathbf{F}_{en}} \end{bmatrix}, \quad \boldsymbol{\psi}_{\hat{\theta}} = \begin{bmatrix} \boldsymbol{\psi}_{\mathbf{F}_{e1}} & \cdots & \boldsymbol{\psi}_{\mathbf{F}_{en}} \end{bmatrix},
\end{aligned} \tag{36}$$

where $\boldsymbol{\psi}$ is the matrix that gathers the shape functions associated to the nodes of the elements and $\boldsymbol{\psi}_{\mathbf{F}_{ef}}$ is the matrix collecting the shape functions associated to the nodes along the sides of the element.

Some notation used to represent the element matrices in case of both HDG and CG is given as follows,

$$\tilde{\boldsymbol{\nabla}} \equiv \begin{bmatrix} \dfrac{\partial}{\partial x_1} & \dfrac{\partial}{\partial x_2} & & \\ & & \dfrac{\partial}{\partial x_1} & \dfrac{\partial}{\partial x_2} \end{bmatrix}, \quad \tilde{\mathbf{N}} \equiv \begin{bmatrix} n_1 & n_2 & & \\ & & n_1 & n_2 \end{bmatrix}. \tag{37}$$

The definition of elemental matrices corresponding to the standard local problem of HDG in the case of coupled CG-HDG formulation for heat equation (13) are presented as follows,

$$\begin{aligned}
\mathbf{A}_{qq}^{(e)} &= \left(\boldsymbol{\psi}_q^T, k_D^{-1}\boldsymbol{\psi}_q\right)_{\Omega^e}, & \mathbf{A}_{q\theta}^{(e)} &= -\left((\tilde{\boldsymbol{\nabla}}^T\boldsymbol{\psi}_q)^T, \boldsymbol{\psi}_\theta\right)_{\Omega^e}, \\
\mathbf{A}_{q\hat{\theta}}^{(e)} &= \langle(\boldsymbol{n}^T\boldsymbol{\psi}_q)^T, \boldsymbol{\psi}_{\hat{\theta}}\rangle_{\partial\Omega^e}, & \mathbf{A}_{\theta q}^{(e)} &= \left(\boldsymbol{\psi}_\theta^T, (\tilde{\boldsymbol{\nabla}}^T\boldsymbol{\psi}_q)^T\right)_{\Omega^e}, \\
\mathbf{A}_{\theta\theta}^{(e)} &= \langle\boldsymbol{\psi}_\theta^T, \tau\boldsymbol{\psi}_\theta\rangle_{\partial\Omega^e}, & \mathbf{A}_{\theta\hat{\theta}}^{(e)} &= -\langle\boldsymbol{\psi}_\theta^T, \tau\boldsymbol{\psi}_{\hat{\theta}}\rangle_{\partial\Omega^e}.
\end{aligned} \tag{38}$$

The matrices of global system of HDG and CG in system (13) are defined as,

$$\begin{aligned}
\mathbf{A}_{\hat{\theta}\hat{\theta}}^{(e)} &= -\langle\boldsymbol{\psi}_{\hat{\theta}}^T, \tau\boldsymbol{\psi}_{\hat{\theta}}\rangle_{\partial\Omega^e}, & \mathbf{A}_{\hat{\theta}\theta}^{(e)} &= \langle\boldsymbol{\psi}_{\hat{\theta}}^T, \tau\boldsymbol{\psi}_\theta\rangle_{\partial\Omega^e}, \\
\mathbf{A}_{\hat{\theta}q}^{(e)} &= \langle\boldsymbol{\psi}_{\hat{\theta}}^T, (\boldsymbol{n}^T\boldsymbol{\psi}_q)\rangle_{\partial\Omega^e}, & \mathbf{K}_{\theta\theta}^{(e)} &= \left((\boldsymbol{\nabla}\boldsymbol{\psi}_\theta^C)^T, k_C\boldsymbol{\nabla}\boldsymbol{\psi}_\theta^C\right)_{\Omega^e}.
\end{aligned} \tag{39}$$

where $\boldsymbol{\psi}_\theta^C$ corresponds to the matrix that has the shape functions of the temperature, θ_C, in Ω_C. Finally, the matrices that arise from the coupling of HDG and CG on the interface, Γ_I, in the equation (13) can be expressed as follows,

$$\begin{aligned}
\mathbf{B}_{\theta\theta}^{(e)} &= -\langle\boldsymbol{\psi}_\theta^T, \tau\boldsymbol{\psi}_\theta^C\rangle_{\partial\Omega^e\cap\Gamma_I}, & \mathbf{B}_{q\theta}^{(e)} &= \langle(\boldsymbol{n}^T\boldsymbol{\psi}_q)^T, \boldsymbol{\psi}_\theta^C\rangle_{\partial\Omega^e\cap\Gamma_I} \\
\mathbf{B}_{\theta q}^{(e)} &= -\mathbf{B}_{q\theta}^{(e)T}
\end{aligned} \tag{40}$$

The definition of elemental matrices that arise from Navier–Stokes equations are already provided in our previous work [38]. The non-linear matrices from the local problem (28) and global problem (29) are defined as follows,

$$\begin{aligned}
\mathbf{C}_{\theta\theta}^{(e)}(\boldsymbol{u}) &= -\langle\boldsymbol{\psi}_{\theta,1}^T, u_1\boldsymbol{\psi}_\theta\rangle_{\partial\Omega^e} - \langle\boldsymbol{\psi}_{\theta,2}^T, u_2\boldsymbol{\psi}_\theta\rangle_{\partial\Omega^e}, \\
\mathbf{C}_{\theta\hat{\theta}}^{(e)}(\hat{\boldsymbol{u}}) &= \langle\boldsymbol{\psi}_\theta^T, (\hat{\boldsymbol{u}}\cdot\boldsymbol{n})\boldsymbol{\psi}_{\hat{\theta}}\rangle_{\partial\Omega^e}, \\
\mathbf{C}_{\hat{\theta}\hat{\theta}}^{(e)}(\hat{\boldsymbol{u}}) &= \langle\boldsymbol{\psi}_{\hat{\theta}}^T, (\hat{\boldsymbol{u}}\cdot\boldsymbol{n})\boldsymbol{\psi}_{\hat{\theta}}\rangle_{\partial\Omega^e}.
\end{aligned} \tag{41}$$

The tangent operators of the non-linear matrices already presented in (41) are given as,

$$\begin{aligned}
\mathbf{C}^{(e)}_{\theta\theta T}(\theta) &= -\left[\langle \boldsymbol{\psi}^T_{\theta,1}, \theta\, \boldsymbol{\psi}_\theta\rangle_{\partial\Omega^e}\ \langle \boldsymbol{\psi}^T_{\theta,2}, \theta\, \boldsymbol{\psi}_\theta\rangle_{\partial\Omega^e}\right], \\
\mathbf{C}^{(e)}_{\theta\hat{\theta}T}(\theta) &= \left[\langle \boldsymbol{\psi}^T_{\theta}, \theta\, n_1\, \boldsymbol{\psi}_{\hat{u}}\rangle_{\partial\Omega^e}\ \langle \boldsymbol{\psi}^T_{\theta}, \theta\, n_2\, \boldsymbol{\psi}_{\hat{u}}\rangle_{\partial\Omega^e}\right], \\
\mathbf{C}^{(e)}_{\hat{\theta}\hat{\theta}T}(\theta) &= \left[\langle \boldsymbol{\psi}^T_{\hat{\theta}}, \theta\, n_1\, \boldsymbol{\psi}_{\hat{u}}\rangle_{\partial\Omega^e}\ \langle \boldsymbol{\psi}^T_{\hat{\theta}}, \theta\, n_2\, \boldsymbol{\psi}_{\hat{u}}\rangle_{\partial\Omega^e}\right].
\end{aligned} \tag{42}$$

References

1. Abramowitz, M.: Handbook of Mathematical Functions, With Formulas, Graphs, and Mathematical Tables. Dover Publications, Incorporated (1974)
2. Alotto, P., Bertoni, A., Perugia, I., Schötzau, D.: Discontinuous finite element methods for the simulation of rotating electrical machines. COMPEL - The international journal for computation and mathematics in electrical and electronic engineering **20**(2), 448–462 (2001). DOI 10.1108/03321640110383320. URL http://dx.doi.org/10.1108/03321640110383320
3. Amestoy, P.R., Davis, T.A., Duff, I.S.: An approximate minimum degree ordering algorithm. SIAM Journal on Matrix Analysis and Applications **17**(4), 886–905 (1996). DOI 10.1137/S0895479894278952. URL http://dx.doi.org/10.1137/S0895479894278952
4. Arioli, M., Demmel, J.W., Duff, I.S.: Solving sparse linear systems with sparse backward error. SIAM Journal on Matrix Analysis and Applications **10**(2), 165–190 (1989). DOI 10.1137/0610013. URL http://dx.doi.org/10.1137/0610013
5. Arnold, D.N.: An interior penalty finite element method with discontinuous elements. SIAM Journal on Numerical Analysis **19**(4), 742–760 (1982). DOI 10.1137/0719052. URL http://dx.doi.org/10.1137/0719052
6. Betts, P.L., Haroutunian, V.: A stream function finite element solution for two-dimensional natural convection with accurate representation of Nusselt number variations near a corner. International Journal for Numerical Methods in Fluids **3**(6), 605–622 (1983). DOI 10.1002/fld.1650030607. URL http://dx.doi.org/10.1002/fld.1650030607
7. Blain, C.A., Massey, T.C.: Application of a coupled discontinuous-continuous Galerkin finite element shallow water model to coastal ocean dynamics. Ocean Modelling **10**(3-4), 283 – 315 (2005). DOI http://dx.doi.org/10.1016/j.ocemod.2004.09.002. URL http://www.sciencedirect.com/science/article/pii/S1463500304000514
8. Cangiani, A., Chapman, J., Georgoulis, E., Jensen, M.: On the Stability of Continuous-Discontinuous Galerkin Methods for Advection-Diffusion-Reaction Problems. Journal of Scientific Computing **57**(2), 313–330 (2013). DOI 10.1007/s10915-013-9707-y. URL http://dx.doi.org/10.1007/s10915-013-9707-y
9. Cockburn, B., Dong, B., Guzmán, J.: A Superconvergent LDG-Hybridizable Galerkin Method for Second-Order Elliptic Problems. Mathematics of Computation **77**(264), 1887–1916 (2008). URL http://www.jstor.org/stable/40234595
10. Cockburn, B., Dong, B., Guzman, J., Restelli, M., Sacco, R.: A hybridizable discontinuous Galerkin method for steady-state convection-diffusion-reaction problems. SIAM Journal on Scientific Computing **31**(5), 3827–3846 (2009). DOI 10.1137/080728810. URL http://dx.doi.org/10.1137/080728810
11. Cockburn, B., Gopalakrishnan, J., Lazarov, R.: Unified hybridization of discontinuous Galerkin, mixed, and continuous Galerkin methods for second order elliptic problems. SIAM Journal on Numerical Analysis **47**(2), 1319–1365 (2009). DOI 10.1137/070706616. URL http://dx.doi.org/10.1137/070706616
12. Cockburn, B., Guzmán, J., Wang, H.: Superconvergent discontinuous Galerkin methods for second-order elliptic problems. Mathematics of Computation **78**(265), 1–24 (2009). URL http://www.ams.org/journals/mcom/2009-78-265/S0025-5718-08-02146-7/home.html;http://www.ams.org/journals/mcom/2009-78-265/S0025-5718-08-02146-7/S0025-5718-08-02146-7.pdf

13. Cockburn, B., Shu, C.: The local discontinuous Galerkin method for time-dependent convection-diffusion systems. SIAM Journal on Numerical Analysis **35**(6), 2440–2463 (1998). DOI 10.1137/S0036142997316712. URL http://dx.doi.org/10.1137/S0036142997316712
14. Dawson, C., Proft, J.: Coupling of continuous and discontinuous Galerkin methods for transport problems. Computer Methods in Applied Mechanics and Engineering **191**(29-30), 3213 – 3231 (2002). DOI http://dx.doi.org/10.1016/S0045-7825(02)00257-8. URL http://www.sciencedirect.com/science/article/pii/S0045782502002578
15. Dawson, C., Proft, J.: Discontinuous and coupled continuous/discontinuous Galerkin methods for the shallow water equations. Computer Methods in Applied Mechanics and Engineering **191**(41-42), 4721 – 4746 (2002). DOI http://dx.doi.org/10.1016/S0045-7825(02)00402-4. URL http://www.sciencedirect.com/science/article/pii/S0045782502004024
16. Dawson, C., Proft, J.: Discontinuous/continuous Galerkin methods for coupling the primitive and wave continuity equations of shallow water. Computer Methods in Applied Mechanics and Engineering **192**(47 - 48), 5123 – 5145 (2003). DOI http://dx.doi.org/10.1016/j.cma.2003.07.004. URL http://www.sciencedirect.com/science/article/pii/S0045782503004833
17. Dawson, C., Proft, J.: Coupled discontinuous and continuous Galerkin finite element methods for the depth-integrated shallow water equations. Computer Methods in Applied Mechanics and Engineering **193**(3 - 5), 289 – 318 (2004). DOI http://dx.doi.org/10.1016/j.cma.2003.09.011. URL http://www.sciencedirect.com/science/article/pii/S0045782503005450
18. De Vahl Davis, G.: Natural convection of air in a square cavity: A bench mark numerical solution. International Journal for Numerical Methods in Fluids **3**(3), 249–264 (1983). DOI 10.1002/fld.1650030305. URL http://dx.doi.org/10.1002/fld.1650030305
19. Dorfman, A.S.: Conjugate Problems in Convective Heat Transfer. CRC Press Taylor & Francis (2009)
20. Geuzaine, C., Remacle, J.F.: Gmsh: a three-dimensional finite element mesh generator with built-in pre- and post-processing facilities. International Journal for Numerical Methods in Engineering **79**(11), 1309–1331 (2009)
21. Giorgiani, G., Fernández-Méndez, S., Huerta, A.: Hybridizable Discontinuous Galerkin with degree adaptivity for the incompressible Navier–Stokes equations. Computers & Fluids **98**, 196 – 208 (2014). DOI http://dx.doi.org/10.1016/j.compfluid.2014.01.011. URL //www.sciencedirect.com/science/article/pii/S0045793014000188. 12th USNCCM mini-symposium of High-Order Methods for Computational Fluid Dynamics - A special issue dedicated to the 80th birthday of Professor Antony Jameson
22. Giorgiani, G., Modesto, D., Fernández-Méndez, S., Huerta, A.: High-order continuous and discontinuous Galerkin methods for wave problems. International Journal for Numerical Methods in Fluids **73**(10), 883–903 (2013). DOI 10.1002/fld.3828. URL http://dx.doi.org/10.1002/fld.3828
23. Hesthaven, J.S., Warburton, T.: Nodal high-order methods on unstructured grids: I. time-domain solution of Maxwell's equations. Journal of Computational Physics **181**(1), 186 – 221 (2002). DOI http://dx.doi.org/10.1006/jcph.2002.7118. URL http://www.sciencedirect.com/science/article/pii/S0021999102971184
24. Holzapfel, G.A.: Nonlinear Solid Mechanics: A Continuum Approach for Engineering. John Wiley & Sons (2000)
25. HSL: A collection of Fortran codes for large scale scientific computation. (2016). URL http://www.hsl.rl.ac.uk/
26. Kaminski, D.A., Prakash, C.: Conjugate natural convection in a square enclosure: effect of conduction in one of the vertical walls. International Journal of Heat and Mass Transfer **29**(12), 1979 – 1988 (1986). DOI http://dx.doi.org/10.1016/0017-9310(86)90017-7. URL http://www.sciencedirect.com/science/article/pii/0017931086900177
27. Kirby, R.M., Sherwin, S.J., Cockburn, B.: To CG or to HDG: A comparative study. Journal of Scientific Computing **51**(1), 183–212 (2012). DOI 10.1007/s10915-011-9501-7. URL http://dx.doi.org/10.1007/s10915-011-9501-7
28. Kovasznay, L.I.G.: Laminar flow behind a two-dimensional grid. Mathematical Proceedings of the Cambridge Philosophical Society **44**, 58–62 (1948).

DOI 10.1017/S0305004100023999. URL http://journals.cambridge.org/article_S0305004100023999
29. LaCaN: EZ4U. Mesh generation environment (2016). URL http://www.lacan.upc.edu/ez4u.htm
30. Le Quéré, P.: Accurate solutions to the square thermally driven cavity at high Rayleigh number. Computers & Fluids **20**(1), 29 – 41 (1991). DOI http://dx.doi.org/10.1016/0045-7930(91)90025-D. URL http://www.sciencedirect.com/science/article/pii/004579309190025D
31. Liu, R., Wheeler, M.F., Dawson, C.N., Dean, R.H.: On a coupled discontinuous/continuous Galerkin framework and an adaptive penalty scheme for poroelasticity problems. Computer Methods in Applied Mechanics and Engineering **198**(41-44), 3499 – 3510 (2009). DOI http://dx.doi.org/10.1016/j.cma.2009.07.005. URL http://www.sciencedirect.com/science/article/pii/S0045782509002473
32. Misra, D., Sarkar, A.: Finite element analysis of conjugate natural convection in a square enclosure with a conducting vertical wall. Computer Methods in Applied Mechanics and Engineering **141**(3), 205 – 219 (1997). DOI http://dx.doi.org/10.1016/S0045-7825(96)01109-7. URL http://www.sciencedirect.com/science/article/pii/S0045782596011097
33. Nguyen, N., Peraire, J., Cockburn, B.: An implicit high-order hybridizable discontinuous Galerkin method for linear convection–diffusion equations. Journal of Computational Physics **228**(9), 3232 – 3254 (2009). DOI http://dx.doi.org/10.1016/j.jcp.2009.01.030. URL http://www.sciencedirect.com/science/article/pii/S0021999109000308
34. Nguyen, N.C., Peraire, J., Cockburn, B.: An implicit high-order hybridizable discontinuous Galerkin method for nonlinear convection–diffusion equations. Journal of Computational Physics **228**(23), 8841 – 8855 (2009). DOI http://dx.doi.org/10.1016/j.jcp.2009.08.030. URL http://www.sciencedirect.com/science/article/pii/S0021999109004756
35. Nguyen, N.C., Peraire, J., Cockburn, B.: High-order implicit hybridizable discontinuous Galerkin methods for acoustics and elastodynamics. Journal of Computational Physics **230**(10), 3695 – 3718 (2011). DOI http://dx.doi.org/10.1016/j.jcp.2011.01.035. URL http://www.sciencedirect.com/science/article/pii/S002199911100060X
36. Nguyen, N.C., Peraire, J., Cockburn, B.: An implicit high-order hybridizable discontinuous Galerkin method for the incompressible Navier–Stokes equations. Journal of Computational Physics **230**(4), 1147 – 1170 (2011). DOI http://dx.doi.org/10.1016/j.jcp.2010.10.032. URL http://www.sciencedirect.com/science/article/pii/S0021999110005887
37. Paipuri, M., Fernández-Méndez, S., Tiago, C.: Comparison of continuous and hybridizable discontinuous Galerkin methods in incompressible fluid flow problems. In: I. Arias, J.M. Blanco, S. Clain, P. Flores, P. Lourenço, J.J. Ródenas, M. Tur (eds.) Congreso de Métodos Numéricos en Ingeniería – CMN 2017. International Center for Numerical Methods in Engineering (CIMNE), Valencia, Spain (2017)
38. Paipuri, M., Fernández-Méndez, S., Tiago, C.: Comparison of high-order continuous and hybridizable discontinuous Galerkin methods in incompressible fluid flow problems. Mathematics and Computers in Simulation (2017). (Submitted)
39. Peraire, J., Persson, P.O.: The compact discontinuous Galerkin (CDG) method for elliptic problems. SIAM Journal on Scientific Computing **30**(4), 1806–1824 (2008). DOI 10.1137/070685518. URL http://dx.doi.org/10.1137/070685518
40. Perugia, I., Schötzau, D.: On the coupling of local discontinuous Galerkin and conforming finite element methods. Journal of Scientific Computing **16**(4), 411–433 (2001). DOI 10.1023/A:1013294207868. URL http://dx.doi.org/10.1023/A:1013294207868
41. Reed, W.H., Hill, T.R.: Triangular mesh methods for the neutron transport equation. Los Alamos Report LA-UR-73-479 (1973)
42. Sarrate, J., Huerta, A.: Efficient unstructured quadrilateral mesh generation. International Journal for Numerical Methods in Engineering **49**(10), 1327–1350 (2000). DOI 10.1002/1097-0207(20001210)49:10⟨1327::AID-NME996⟩3.0.CO;2-L. URL http://dx.doi.org/10.1002/1097-0207(20001210)49:10<1327::AID-NME996>3.0.CO;2-L
43. Sarrate, J., Huerta, A.: Generación automática de mallas no estructuradas y formadas exclusivamente por cuadriláteros sobre superficies curvas en $\mathbb{R}^3$. Revista Internacional de Métodos Numéricos para Cálculo y Diseño en Ingeniería **18**(1), 79–93 (2002)

44. Sevilla, R., Huerta, A.: Tutorial on Hybridizable Discontinuous Galerkin (HDG) for Second-Order Elliptic Problems, pp. 105–129. Springer International Publishing (2016). DOI 10.1007/978-3-319-31925-4_5. URL http://dx.doi.org/10.1007/978-3-319-31925-4_5
45. Taylor, C., Hood, P.: A numerical solution of the Navier–Stokes equations using the finite element technique. Computers & Fluids **1**(1), 73–100 (1973)
46. Taylor, M.A., Wingate, B.A., Vincent, R.E.: An algorithm for computing Fekete points in the triangle. SIAM Journal on Numerical Analysis **38**(5), 1707–1720 (2000). DOI 10.1137/S0036142998337247. URL http://dx.doi.org/10.1137/S0036142998337247
47. William, W.H.: Condition estimates. SIAM Journal on Scientific and Statistical Computing **5**(2), 311–316 (1984). DOI 10.1137/0905023. URL http://dx.doi.org/10.1137/0905023
48. Yakovlev, S., Moxey, D., Kirby, R.M., Sherwin, S.J.: To CG or to HDG: A comparative study in 3D. Journal of Scientific Computing **67**(1), 192–220 (2016). DOI 10.1007/s10915-015-0076-6. URL http://dx.doi.org/10.1007/s10915-015-0076-6
49. Zarin, H.: Continuous-discontinuous finite element method for convection-diffusion problems with characteristic layers. Journal of Computational and Applied Mathematics **231**(2), 626 – 636 (2009). DOI http://dx.doi.org/10.1016/j.cam.2009.04.010. URL http://www.sciencedirect.com/science/article/pii/S0377042709002623
50. Zhu, P., Xie, Z., Zhou, S.: A uniformly convergent continuous-discontinuous Galerkin method for singularly perturbed problems of convection-diffusion type. Applied Mathematics and Computation **217**(9), 4781 – 4790 (2011). DOI http://dx.doi.org/10.1016/j.amc.2010.11.033. URL http://www.sciencedirect.com/science/article/pii/S0096300310011458
51. Zhu, P., Ziqing, X., Shuzi, Z.: A coupled continuous-discontinuous FEM approach for convection diffusion equations. Acta Mathematica Scientia **31**(2), 601 – 612 (2011). DOI http://dx.doi.org/10.1016/S0252-9602(11)60260-9. URL http://www.sciencedirect.com/science/article/pii/S0252960211602609